2015

ELECTRON-BEAM PATTERNING OF TEFLON AF FOR SURFACE PLASMON RESONANCE SENSING

Mansoor A. Sultan
University of Kentucky, m.sultan@uky.edu

STUDENT AGREEMENT:

I represent that my thesis or dissertation and abstract are my original work. Proper attribution has been given to all outside sources. I understand that I am solely responsible for obtaining any needed copyright permissions. I have obtained needed written permission statement(s) from the owner(s) of each third-party copyrighted matter to be included in my work, allowing electronic distribution (if such use is not permitted by the fair use doctrine) which will be submitted to UKnowledge as Additional File.

I hereby grant to The University of Kentucky and its agents the irrevocable, non-exclusive, and royalty-free license to archive and make accessible my work in whole or in part in all forms of media, now or hereafter known. I agree that the document mentioned above may be made available immediately for worldwide access unless an embargo applies.

I retain all other ownership rights to the copyright of my work. I also retain the right to use in future works (such as articles or books) all or part of my work. I understand that I am free to register the copyright to my work.

REVIEW, APPROVAL AND ACCEPTANCE

The document mentioned above has been reviewed and accepted by the student's advisor, on behalf of the advisory committee, and by the Director of Graduate Studies (DGS), on behalf of the program; we verify that this is the final, approved version of the student's thesis including all changes required by the advisory committee. The undersigned agree to abide by the statements above.

Mansoor A. Sultan, Student

Dr. J. Todd Hastings, Major Professor

Dr. Cai-Cheng Lu, Director of Graduate Studies

ELECTRON-BEAM PATTERNING OF TEFLON AF FOR SURFACE PLASMON RESONANCE SENSING

THESIS

A thesis submitted in partial fulfillment
of the requirements for the degree of
Master of Science in Electrical
Engineering in the College of
Engineering at the University of
Kentucky

By
Mansoor Sultan
Lexington, Kentucky

Director: Dr. J. Todd Hastings, Professor of Electrical Engineering
Lexington, Kentucky 2015

ABSTRACT OF THESIS

ELECTRON-BEAM PATTERNING OF TEFLON AF FOR SURFACE PLASMON RESONANCE SENSING

Variable pressure electron beam etching and lithography for Teflon AF has been demonstrated. The relation between dose and etching depth is tested under high vacuum and water vapor. High resolution structures as small as 75 nm half-pitch have been resolved. Several simulation tools were tested for surface plasmon excitation. Grating based dual mode surface plasmon excitation has been shown numerically and experimentally.

KEYWORDS: Dual Mode Surface Plasmon, Grating Based SPR, VP-EBL, Teflon AF patterning, Simulation.

Author's signature: Mansoor Sultan

Date: April 30, 2015

ELECTRON-BEAM PATTERNING OF TEFLON AF FOR SURFACE PLASMON RESONANCE SENSING

By
Mansoor Sultan

Director of Thesis: J. Todd Hastings

Director of Graduate Studies: Cai-Cheng Lu

Date: April 30, 2015

To my father and my family.

ACKNOWLEDGMENTS

I would never have been able to reach this stage without the guidance of my advisor, help from friends, and support from my family and wife.

I would like to express my gratitude to my advisor, Dr. Hastings, for his guidance, patience, and being available anytime I needed him.

I would like to thank Dr. Vijay Singh and Dr. Janet Lumpp for accepting to be on my thesis defense committee.

I would also like to acknowledge National Science Foundation (NSF) and Jack and Linda Gill Foundation for funding this work.

I would like to acknowledge The Higher Committee for Education Development in Iraq (HCED) for supporting me to be here.

This work would be far more challenging without the help and guidance of my colleagues in the Lab. Dr. Neha Nehru helped me to get started with surface plasmon theory and she was my second resource after Dr. Hastings. Working with Dr. Lindsay Boehme was very useful and her knowledge in chemistry and lithography was a great resource for me. Dr. Carlos Jarro helped me to do my first surface plasmons excitation experiment. Samaneh Esfandiarp and Adham Noubani, my classes and Lab colleagues, with them this journey was more enjoyable, and they were always motivated to help and encourage me.

I would like to thank Mr. Brain Wajdyk, Jacob Hempel for training and guidance at Center for Nanoscale Science and Engineering (CeNSE).

I would also like to thank my family and friend for their continuous support.

Finally, and most importantly, I would like to thank my wife Rasha, she was always there with me in good and bad times.

TABLE OF CONTENTS

Acknowledgments . . . iii

Table of Contents . . . iv

List of Tables . . . vi

List of Figures . . . vii

Chapter 1 : Surface Plasmon Resonance Principles . . . 1
1.1 Introduction . . . 1
1.2 Fundamentals of Surface plasmon . . . 3
1.3 Optical excitation of surface plasmon . . . 4
1.3.1 Prism configuration . . . 4
1.3.2 Grating configuration . . . 11
1.4 Surface plasmon resonance sensors . . . 14

Chapter 2 : Teflon AF Patterning for Surface Plasmon Sensing . . . 17
2.1 Introduction . . . 17
2.2 Teflon AF patterning with variable pressure electron beam lithography (VP-EBL) . . . 18
2.2.1 Sample preparation and Teflon AF thin film coating . . . 19
2.2.2 Lithography process . . . 21

Chapter 3 : Sensor Design and Fabrication. . . . 29
3.1 Simulation tools . . . 29
3.1.1 OptiScan . . . 30
3.1.2 S4: Stanford stratified structure solver . . . 32
3.1.3 PhotonicsSHA 2D . . . 34
3.2 Sensor chip design and fabrication . . . 35

Chapter 4 : Results and Discussion . . . 38
4.1 Experimental setup . . . 38
4.2 Experimental results . . . 39
4.3 Simulation results . . . 42
4.4 Discussion . . . 46

Chapter 5 : Conclusion and Future Work . . . 48
5.1 Conclusion . . . 48
5.2 Future Work . . . 49

Appendix A . . . 50

References 51

Vita 53

LIST OF TABLES

3.1 Exposure conditions for sensor fabrication. 37

LIST OF FIGURES

1.1 The surface plasmon oscillations and electromagnetic fields 2
1.2 Magnetic field exponential decay with the distance from interface in both medium 2
1.3 Kretschmann geometry of the attenuated total reflection (ATR) method for optical surface plasmon excitation. 5
1.4 The effective refractive index of a surface plasmon at a metal-dielectric interface, with gold thickness of 50 nm and different angle of incidence. 6
1.5 The reflectance of TM wave as a function of wavelength for a 500 nm Teflon AF film coated with 55 nm gold film, with incident light through a BK7 prism at 65° incident angle inside the prism. 7
1.6 The reflectance as a function of angle of incidence for a 500 nm Teflon AF film coated with 55 nm gold film with incident light through a BK7 prism of a wavelength 650 nm. 8
1.7 Otto geometry of the attenuated total reflection (ATR) method for optical surface plasmon excitation. 9
1.8 Field profile for symmetric and antisymmetric modes of surface plasmon wave. 10
1.9 The dispersion relation for the surface plasmon modes of a thin metal film between two dielectrics. The metal thickness of 50 nm and the angle of incidence is 66.5° and the light incident through a BK7 prism. 10
1.10 Reflectance as function of wavelength for a 500 nm Teflon AF film coated with a 55 nm gold film with incident light through a BK7 prism at a 65° incident angle for dual mode excitation. 11
1.11 Grating based surface plasmon excitation configuration. 12
1.12 Normalized wave vectors for surface plasmon wave and first positive ($m = +1$) diffracted wave as a function of wavelength and angle of incidence. 13
1.13 Dual surface plasmon excitation with grating configuration 14
1.14 Block diagram of optical SPR sensor. 15

2.1 Chemical structure of Teflon AF [1]. 17
2.2 Teflon AF patterning process, ... 18
2.3 Teflon AF film thickness as function of spinning speed and dilution ratio. . . . 20
2.4 Teflon AF refractive index as function of wavelength measured by ellipsometry. 20
2.5 Dose vs. Depth for e-beam exposure of Teflon AF using [a] 10 keV, [b] 20 keV, and [c] 30 keV beam energies under high-vacuum and 1 Torr water vapor conditions before and after development. 22
2.6 Threshold and contrast estimation plot for 1 Torr water vapor condition after development [a] 10 keV, [b] 20 keV, and [c] 30 keV. 24
2.7 Nested lines with 750 nm half-pitch, exposed with a beam energy of 10 keV and a dose of $1,300\ pC/cm$ with 1 Torr H_2O pressure. 25
2.8 Nested lines with 150 nm half-pitch, exposed with beam energy of 10 keV and a dose of $5,200\ pC/cm$ with 1 Torr H_2O pressure. 26

2.9 Nested lines with 75 nm half-pitch, exposed with beam energy 10 keV and a dose of $5,200\ pC/cm$ with 1 Torr H_2O pressure. 27
2.10 Nested lines with 38 nm half-pitch, exposed with beam energy 10 keV and a dose of $1,300\ pC/cm$ with 1 Torr H_2O pressure. 28

3.1 Design tested with OptiScan. 31
3.2 Diffraction efficiency as a function of wavelength and number or orders for the grating structure in Figure (3.1). 32
3.3 Reflectance as a function of wavelength and number of orders for the grating structure in Figure (3.1) tested with the S4 tool from the nanohub website. . . . 33
3.4 Diffraction efficiency as a function of wavelength and number of orders for the grating structure in Figure (3.1) tested with PhotonicsSHA 2D. 35
3.5 Grating period test for dual mode excitation with grating structure. 36

4.1 Experimental setup for sensor chip testing. 39
4.2 SEM image for a grating structure that supports dual surface plasmons excitation. The grating period is 430 nm. The image was taken after the optical measurements due to carbon deposition and etching of the Teflon with high beam energies. 40
4.3 Experimental results for reflectance as a function of wavelength for TE and TM modes for the grating shown in Figure(4.2). The TM mode shows single mode excitation for SPR around 630 nm. 41
4.4 Experimental results for reflectance as a function of wavelength for TE and TM modes for the grating shown in Figure(4.2). The TM mode shows SRSP and LRSP excitation at 590 nm and 645 nm, respectively. 42
4.5 Dispersion relation for surface plasmon excitation [a] Single mode, [b] Dual mode. 43
4.6 Approximate design for the grating structure in Figure (4.2) was used for simulation with PhotonicsSHA 2D. 44
4.7 TM to TE ratio as function of wavelength for experimental and simulation results [a] Single mode, [b] Dual mode. 45
4.8 Refractive index for water and Teflon as function of wavelength. 46
4.9 TM to TE ratio as a function of wavelength and grating depth simulated by PhotonicsSHA 2D for a 430 nm grating period with different depths. 47

Chapter 1 : Surface Plasmon Resonance Principles

1.1 Introduction

In 1902, Wood observed sharp dark bands in the diffracted light from a metallic diffraction grating, and he called them as anomalies [2]. Fifty-six years later, Thurbadar identified a complete adsorption in the reflectivity of a thin metal film [3]. However, both of them did not identify these observation as surface plasmon resonance (SPR). In 1968, Otto explained similar results; the drop in reflectivity of the thin metal film was due to SPR [4]. The derivation of surface plasmon is based on the plasma configuration of Maxwell's equations, where the free electrons of the metal are considered as the plasma. Plasma oscillation in metals is aggregative longitudinal excitations of the conductive electron gas (see Figure (1.1)), and plasmon are the quanta that represent these charge-density oscillations. The charge-density fluctuations can be exist in the bulk media or bound at metal-dielectric interface, where they spread as waves along the interface forming what called surface plasmon. The propagating electron density oscillations create surface-localized electromagnetic waves. The electromagnetic fields of these waves is perpendicular to the boundary, and they exponentially decay as they propagate in the medium as shown in Figure (1.2). These electromagnetic fields are produced optically under the conditions of total internal reflection at the boundary between the metal and dielectric media. However, the electric and magnetic fields do not stop at the boundary. Rather they propagate into the medium as a surface wave. Despite the fact that Maxwell's equations explained the presence of surface waves and demonstrated them in the first decade of the twentieth century, the surface plasmon field had not been studied until 1960, and the term 'surface plasmon' was coined later in the 1960s. It was proven that Maxwell's equations can solve the surface plasmon field under two conditions. First, one of the media has to have a negative real part of its complex dielectric constant ε. Second, the component of the wave vector (which will be refereed to later as k_x) along

the interface between these two media, must fulfill an equation that includes the dielectric constants of both media [5].

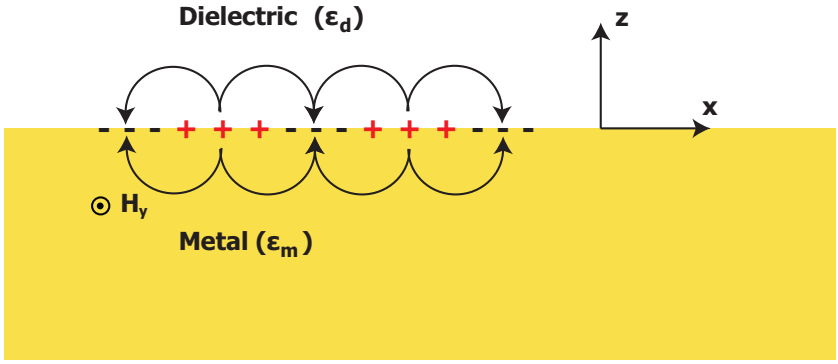

Figure 1.1: The surface plasmon oscillations and electromagnetic fields

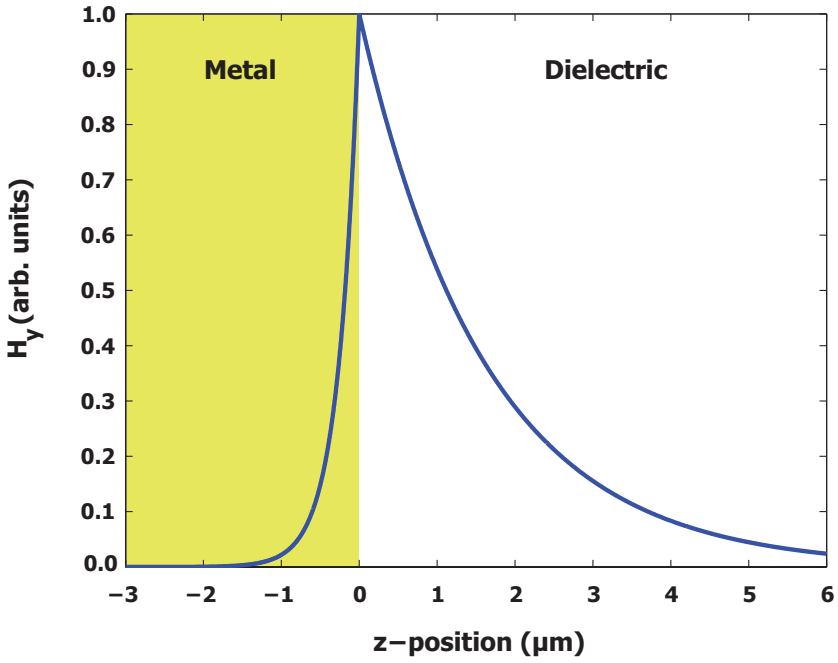

Figure 1.2: Magnetic field exponential decay with the distance from interface in both medium

1.2 Fundamentals of Surface plasmon

If we assume the two media have semi-infinite length (x),oscillations on the boundary between the two media have electromagnetic fields that can be described by the following equations, and depicted in Figure (1.2):

$$\begin{aligned} H_{yd} &= H_0\, e^{(-\gamma_d\, z)}\, e^{(-jk_x\, x)}\ for\ z>0 \\ E_{xd} &= E_0\, e^{(-\gamma_d\, z)}\, e^{(-jk_x\, x)}\ for\ z>0 \\ H_{ym} &= H_0\, e^{(+\gamma_m\, z)}\, e^{(-jk_x\, x)}\ for\ z<0 \\ E_{xm} &= E_0\, e^{(+\gamma_m\, z)}\, e^{(-jk_x\, x)}\ for\ z<0 \end{aligned} \tag{1.1}$$

With

$$\gamma_d = \sqrt{k_x - \varepsilon_d k_0^2}$$
$$\gamma_m = \sqrt{k_x - \varepsilon_m k_0^2}$$

where $k_0 = \frac{2\pi}{\lambda} = \frac{\omega}{c}$ (free space wave vector) and $k_x = k_0\, n_{eff}$

By introducing the dielectric constants for the active surface plasmon medium (metal) as ε_m ($\varepsilon_m = \varepsilon'_m + j\varepsilon''_m$) and ε_d for the adjacent medium (dielectric), and solving Maxwell's equations and boundary conditions we get:

$$k_x^2 + \gamma_d^2 = \varepsilon_m \left(\frac{\omega}{c}\right)^2$$

$$k_x^2 + \gamma_m^2 = \varepsilon_d \left(\frac{\omega}{c}\right)^2$$

and by solving for wave vector k_x we get:

$$k_x = \frac{\omega}{c}\sqrt{\frac{\varepsilon_m \varepsilon_d}{\varepsilon_m + \varepsilon_d}} \tag{1.2}$$

where c is the speed of light in vacuum and ω is the angular frequency of surface plasmon wave. from the equation above we can conclude

$$n_{eff} = \sqrt{\frac{\varepsilon_m \varepsilon_d}{\varepsilon_m + \varepsilon_d}} \tag{1.3}$$

1.3 Optical excitation of surface plasmon

Surface plasmons can be excited with different methods, such as prism coupling [4, 6], grating coupling [7] and waveguide coupling [8]. The most common ways for surface plasmon resonance sensing are the prism and grating configuration; therefore, we will discuss these methods only.

1.3.1 Prism configuration

In the last section, we mentioned that Maxwell's equations have a solution for surface plasmon only when one of the media has a negative real part of its dielectric constant. For this reason, this condition is valid in gold and silver over specific wavelength range. Furthermore, in order to excite surface plasmon by light, the electric field has to have a continuous tangential component along the interface and wave vector match the surface plasmon wave vector (k_x). The later (k_x) is given by equation (1.3) [5]. In the prism coupling, there are two geometries: Kretschmann geometry [6] and Otto geometry [4]. Both configurations depend on a prism coupler and the attenuated total reflection method (ATR). Kretschmann geometry consists of a metal-dielectric interface coupled with a prism, which is shown in Figure (1.3) below. The material propertes in this thesis for the gold and glass are taken from references [9, 10]. Teflon AF optical properties were determined using the Cauchy formula for dispersion fit to the measurements of Lowry *et al.* [11].

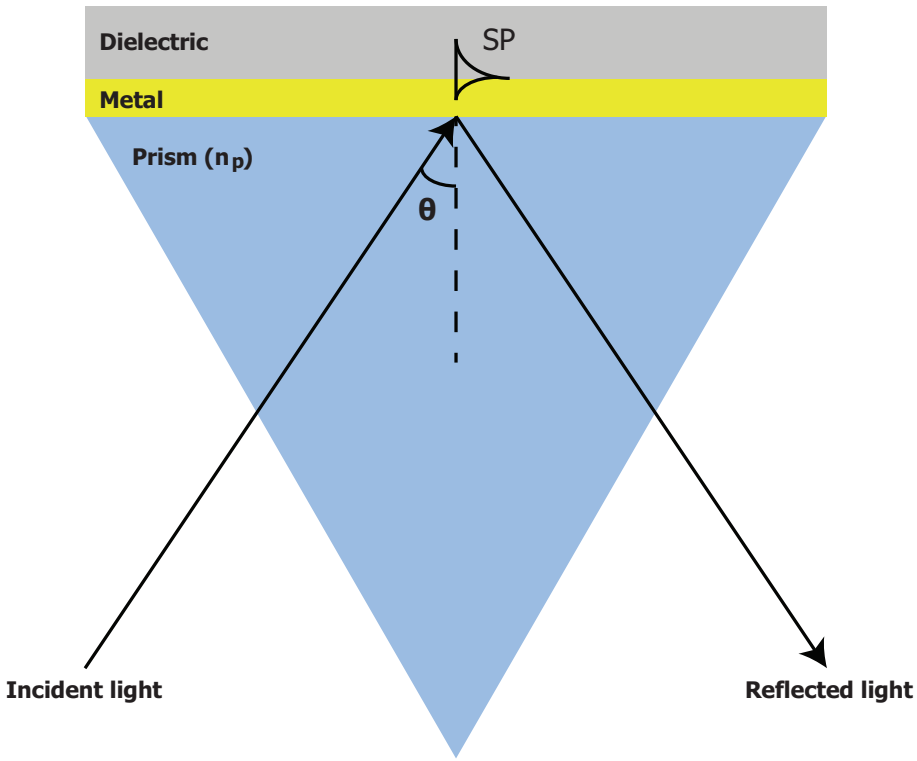

Figure 1.3: Kretschmann geometry of the attenuated total reflection (ATR) method for optical surface plasmon excitation.

When the light penetrates through the prism and reflects from the surface of the metal film, part of this light propagates in the metal film as an evanescent electromagnetic field. The evanescent field couples with surface plasmon at the boundary with the dielectric layer. This coupling only happens when the metal film is adequately thin.The wave vector of the surface plasmon penetrating the metal layer, K_{SP}, is affected by the dielectric layer and has the following formula:

$$k_{SP} = k_{SP0} + \Delta k = \frac{\omega}{c}\sqrt{\frac{\varepsilon_m \varepsilon_d}{\varepsilon_m + \varepsilon_d}} + \Delta k \tag{1.4}$$

Where Δk is the effect of prism and metal thickness.

As we mentioned before, surface plasmon can only be excited when the evanescent wave vector (k_{EW}) matches the surface plasmon vector (k_{SP}):

$$k_{EW} = k_{SP}$$

$$k_{EW} = \frac{2\pi}{\lambda} n_p \sin\theta$$

$$K_{SP} = Re\left\{\frac{2\pi}{\lambda}\sqrt{\frac{\varepsilon_m \varepsilon_d}{\varepsilon_m + \varepsilon_d}}\right\}$$

where n_p is the refractive index of the prism and θ is the angle of incident inside the prism.

$$\frac{2\pi}{\lambda} n_p \sin\theta = Re\left\{\frac{2\pi}{\lambda}\sqrt{\frac{\varepsilon_m \varepsilon_d}{\varepsilon_m + \varepsilon_d}}\right\} + \Delta k \tag{1.5}$$

Solving for the effective refractive index:

$$n_p \sin\theta = n_{eff} + \Delta n = Re\left\{\sqrt{\frac{\varepsilon_m \varepsilon_d}{\varepsilon_m + \varepsilon_d}}\right\} + \Delta n \tag{1.6}$$

Where the condition for surface plasmon excitation is shown in Figure (1.4).

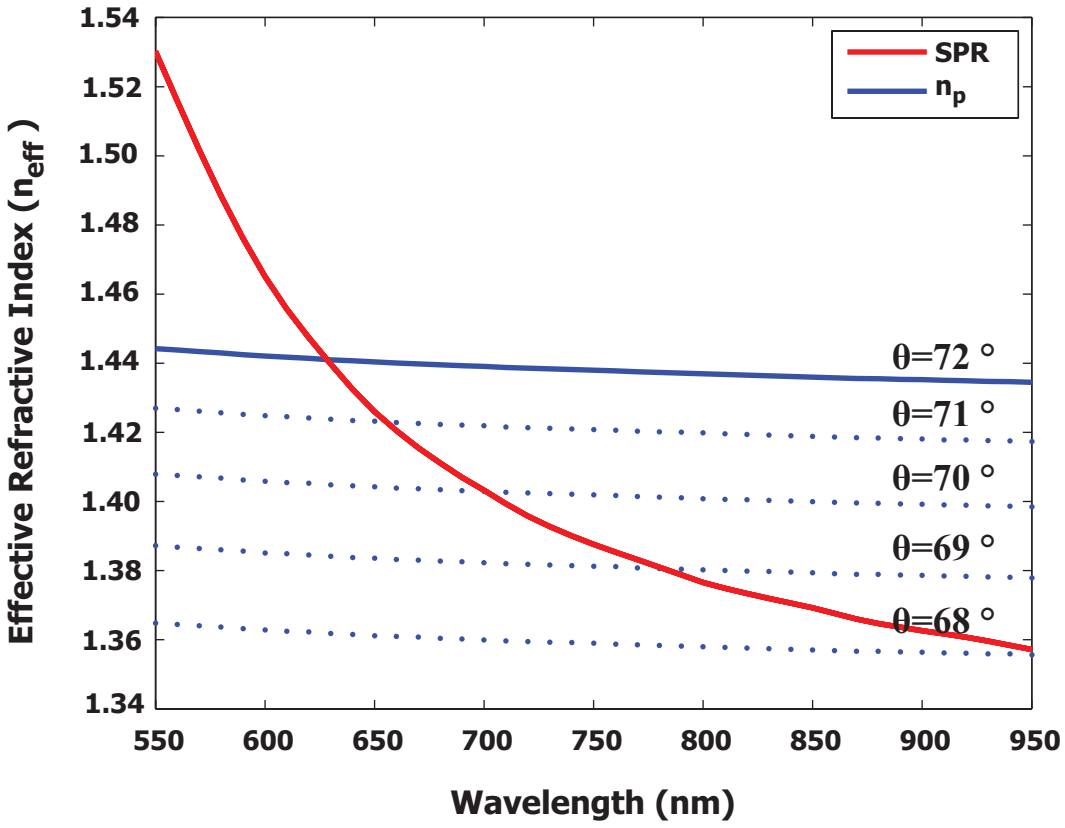

Figure 1.4: The effective refractive index of a surface plasmon at a metal-dielectric interface, with gold thickness of 50 nm and different angle of incidence.

We can see the effect on light reflectance by Kretschmann geometry as shown in Figure (1.5).

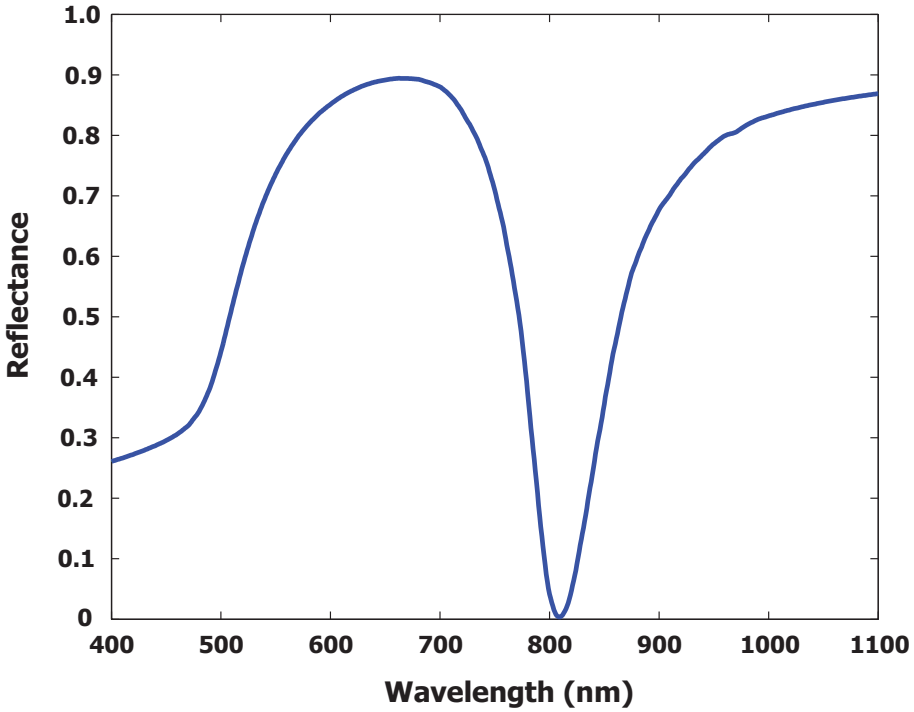

Figure 1.5: The reflectance of TM wave as a function of wavelength for a 500 nm Teflon AF film coated with 55 nm gold film, with incident light through a BK7 prism at 65° incident angle inside the prism.

If we choose a wavelength where the real part of the dielectric of metal is negative, and sweep the angle of incidence the surface plasmon excitation will occurs at specific angle that satisfy equation(1.6) as shown in the Figure (1.6) below.

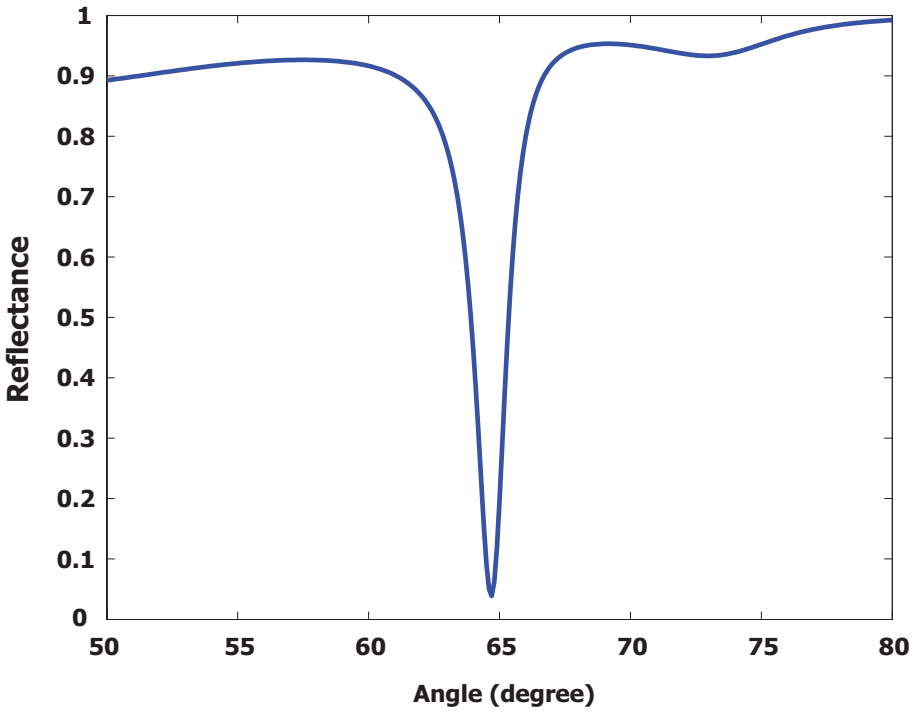

Figure 1.6: The reflectance as a function of angle of incidence for a 500 nm Teflon AF film coated with 55 nm gold film with incident light through a BK7 prism of a wavelength 650 nm.

In Otto geometry, the layers have a different arrangement which is shown in Figure (1.7). There is a few microns gap between the prism and metal. In order to satisfy the coupling condition, the evanescent wave and plasmon wave have to have equal wave vectors. The derivation of surface plasmon wave vector follows the Kretschmann geometry.

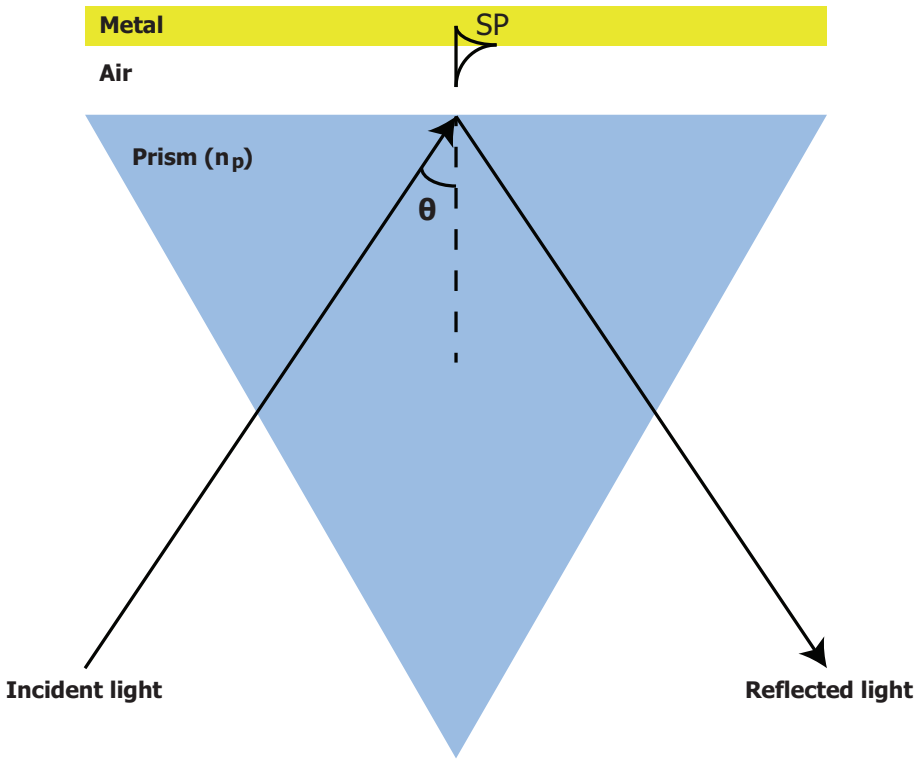

Figure 1.7: Otto geometry of the attenuated total reflection (ATR) method for optical surface plasmon excitation.

Radan *et al.* and Hastings *et al.* have reported more advanced sensor design by exciting symmetric and antisymmetric surface plasmons, or what are called short range surface plasmon (SRSP) and long range surface plasmon (LRSP) [12, 13]. This excitation was achieved by upgrading Kretschmann geometry by introducing a dielectric layer between the prism and metal layer with optical properties that match the dielectric layer on top. The field profile of symmetric and antisymmetric modes is shown in Figure (1.8). The excitation for dual modes occurs when the metal thickness is less than 100 nm. The matching condition for the effective refractive index and the two modes is shown in Figure (1.9), and the reflectance curve as function of wavelength is shown in Figure (1.10)

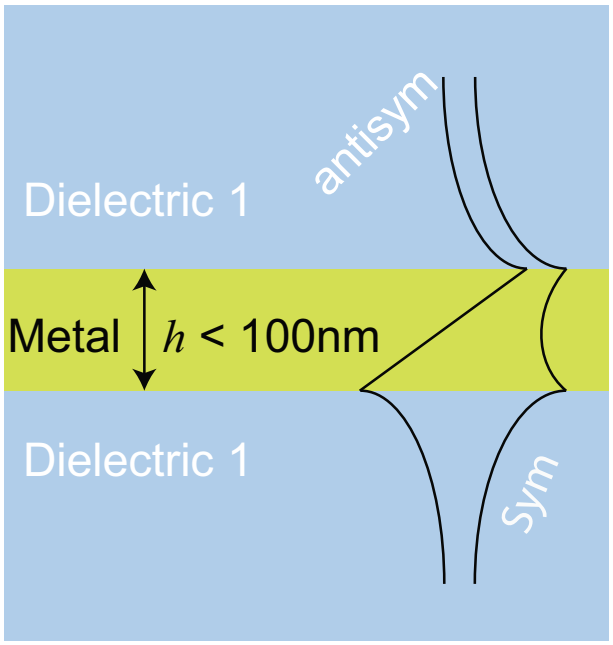

Figure 1.8: Field profile for symmetric and antisymmetric modes of surface plasmon wave.

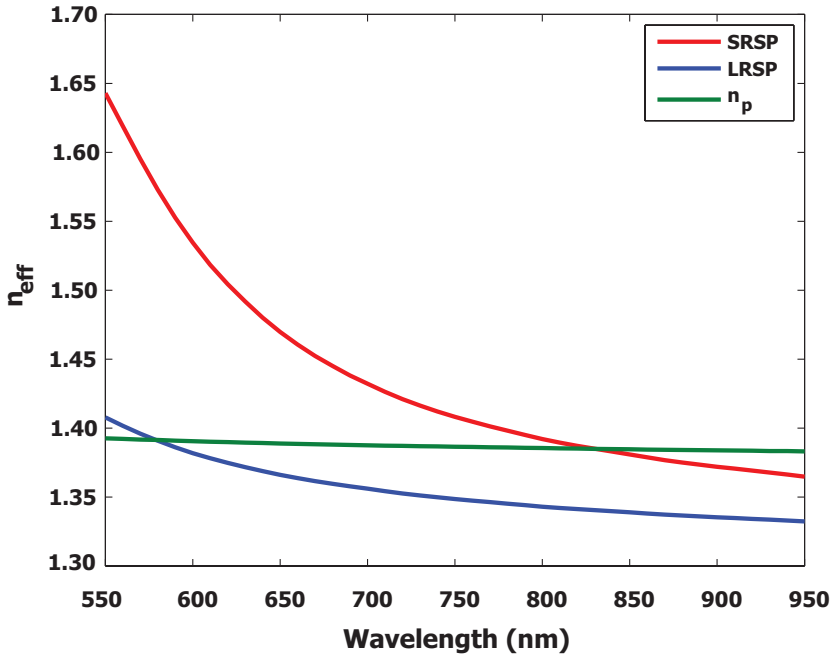

Figure 1.9: The dispersion relation for the surface plasmon modes of a thin metal film between two dielectrics. The metal thickness of 50 nm and the angle of incidence is 66.5° and the light incident through a BK7 prism.

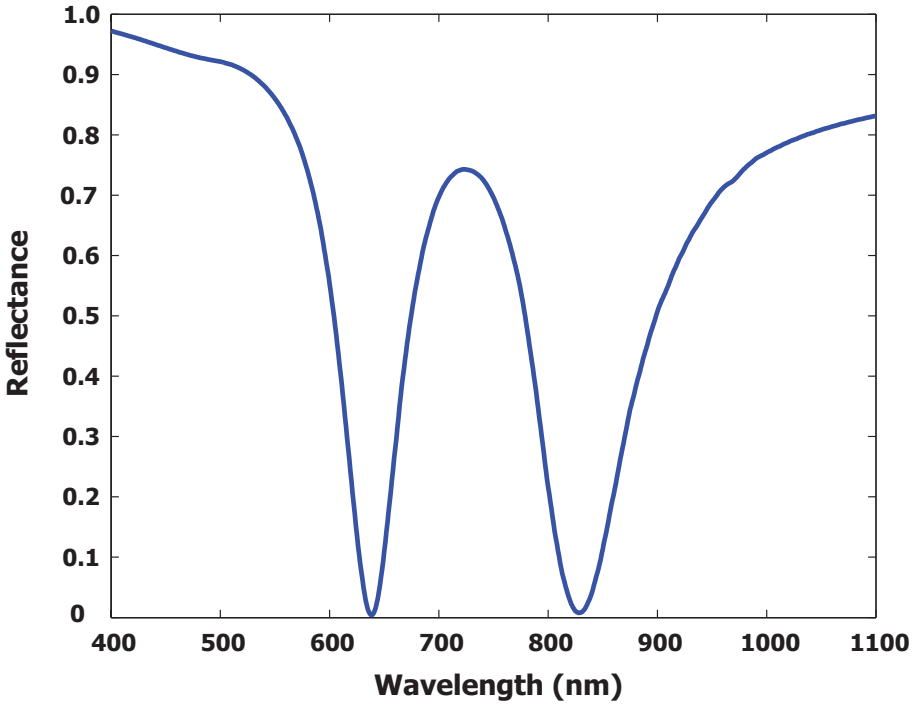

Figure 1.10: Reflectance as function of wavelength for a 500 nm Teflon AF film coated with a 55 nm gold film with incident light through a BK7 prism at a 65° incident angle for dual mode excitation.

1.3.2 Grating configuration

The other common method for surface plasmon excitation is a metal grating. In this configuration, the incident light from dielectric medium on a metal grating with period Λ is shown in Figure (1.11). The wave vector of the diffracted wave must match the wave vector of the surface plasmon wave:

$$k_{diff} = \frac{2\pi}{\lambda} n_d \sin\theta + m\frac{2\pi}{\Lambda} \tag{1.7}$$

$$k_{sp} = \pm\frac{2\pi}{\lambda} Re\left\{\sqrt{\frac{\varepsilon_m \varepsilon_d}{\varepsilon_m + \varepsilon_d}}\right\} + \Delta k \tag{1.8}$$

$$\frac{2\pi}{\lambda} n_d \sin\theta + m\frac{2\pi}{\Lambda} = \pm\frac{2\pi}{\lambda} Re\left\{\sqrt{\frac{\varepsilon_m \varepsilon_d}{\varepsilon_m + \varepsilon_d}}\right\} + \Delta k \tag{1.9}$$

Where n_d is the refractive index of dielectric, θ is angle of incident wave, λ is incident wavelength, Δk is the effect of presence of grating, and m is the diffraction order. Re-arranging the equation above, we get:

$$n_d \sin\theta + m\frac{\lambda}{\Lambda} = \pm Re\left\{\sqrt{\frac{\varepsilon_m \varepsilon_d}{\varepsilon_m + \varepsilon_d}}\right\} + \Delta\, n_{eff} \tag{1.10}$$

where

$$\Delta\, n_{eff} = Re\left\{\frac{\Delta k \lambda}{2\pi}\right\}$$

$$n_{eff} = \pm Re\left\{\sqrt{\frac{\varepsilon_m \varepsilon_d}{\varepsilon_m + \varepsilon_d}}\right\} + \Delta\, n_{eff} \tag{1.11}$$

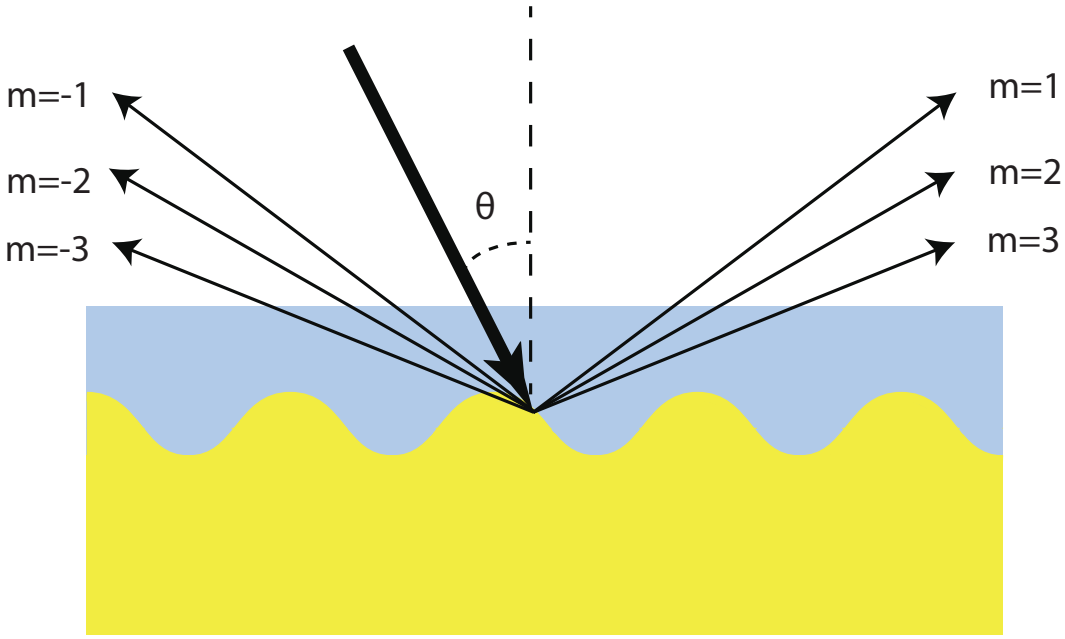

Figure 1.11: Grating based surface plasmon excitation configuration.

Referring to the previous equations (1.9,1.10), it can be seen that the coupling condition can be achieved with different design. For example, if we consider grating made of gold with a period ($\Lambda = 680\ nm$) and incident light from water with a variable angle, we get coupling at different wavelengths as shown in Figure (1.12).

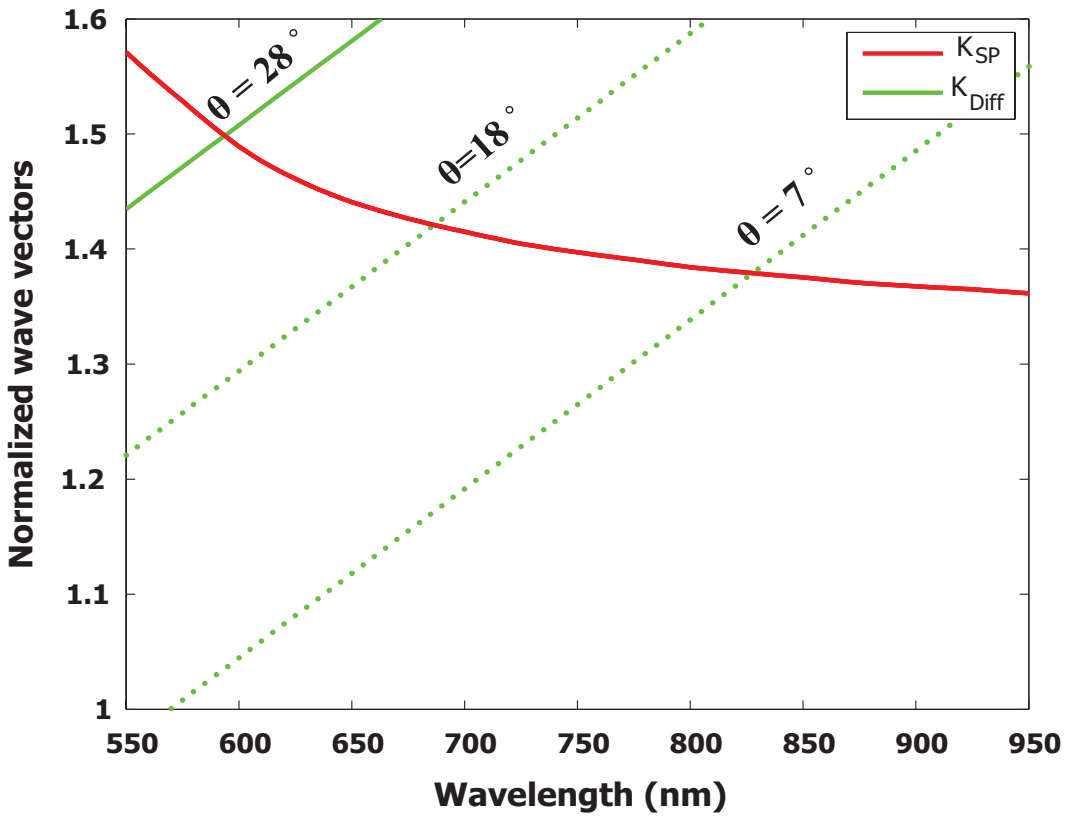

Figure 1.12: Normalized wave vectors for surface plasmon wave and first positive ($m = +1$) diffracted wave as a function of wavelength and angle of incidence.

Vala *et al.* have reported dual mode excitation for SRSP and LRSP with a grating configuration and employed them for SPR sensing [14]. The excitation theory of the symmetric and antisymmetric is identical to the prism configuration, a dielectric grating is coated with a thin metal film. Hence, the matching condition similar to grating configuration and depends on the grating period and modulation of the grating. Dual mode excitation with a diffraction grating is shown in Figure (1.13).

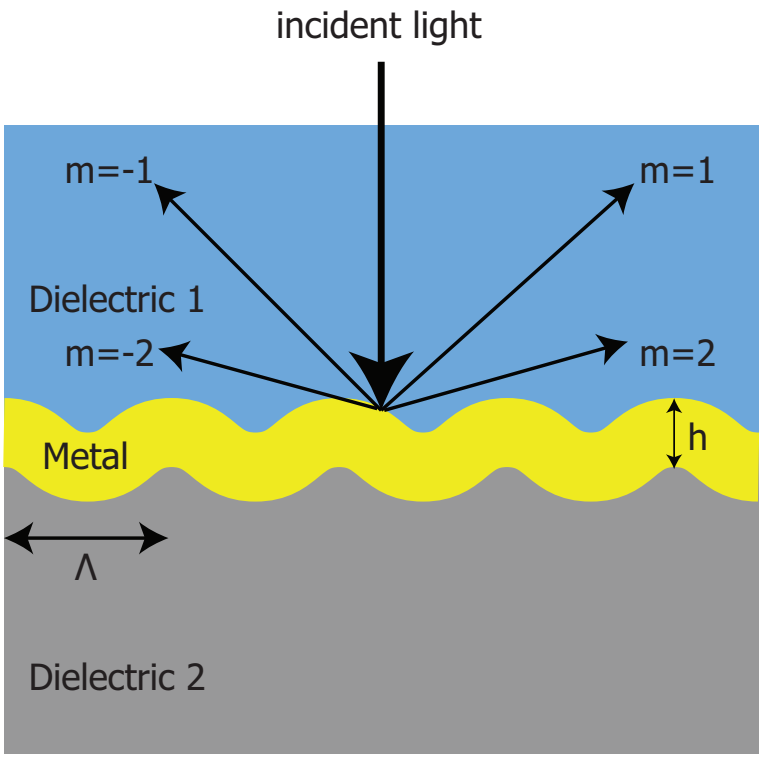

Figure 1.13: Dual surface plasmon excitation with grating configuration .

1.4 Surface plasmon resonance sensors

The use of surface plasmon for optical sensing dates back to the early of 1980s, when surface plasmon sensors were used for studying electrochemical reactions [15]. Many surface plasmon resonance (SPR) sensors have been developed since then. The optical SPR sensor is an instrument composed of light source, a detector, a sensor-chip, an analyte injection unit, and a data processing unit (see Figure (1.14)). As mentioned previously, the excitation of surface plasmon causes changes in the output light properties. SPR sensors can be utilized to sense changes in light properties, and depending on the affected property, the SPR can be interrogated by detecting changes in wavelength, angle, intensity, phase, or polarization. The first three types of interrogation are the most common [16].

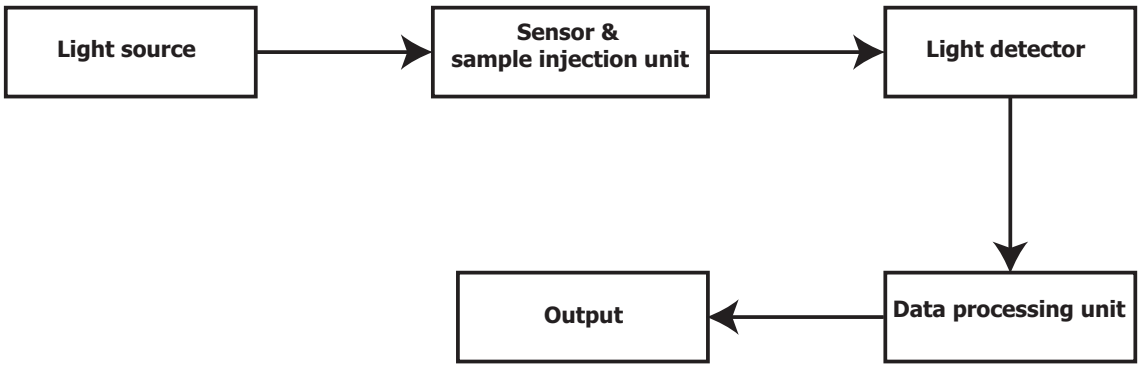

Figure 1.14: Block diagram of optical SPR sensor.

The principle of SPR, as indicated before, depends on the variations of the output light. These variations occur when the refractive index of the dielectric layer changes near the metal surface. The shift in the refractive index happens due to the binding of specific elements to the metal surface or variations of the bulk refractive index for the dielectric layer. Therefore, SPR sensors are considered label-free sensors. The main characteristics of surface plasmon sensor are the sensitivity and limit of detection (LOD), where the first is defined as the ratio between the change of input of sensor to the change of the output. In surface plasmon case, the change in input is the change of refractive index, the change of refractive index happen due to the bulk change or surface binding. Therefore, the sensitivity can be classified into two types: bulk sensitivity (S_B) and surface sensitivity (S_S), which are given in equations(1.12- 1.13).

$$S_B = \frac{\delta \lambda_{SP}}{\delta n} \left(\frac{nm - wavelength}{RIU} \right)$$

$$S_B = \frac{\delta \theta_{SP}}{\delta n} \left(\frac{degree}{RIU} \right) \tag{1.12}$$

$$S_S = \frac{\delta \lambda_{SP}}{t} \left(\frac{nm - wavelength}{nm - binding\ thickness} \right)$$

$$S_S = \frac{\delta \theta_{SP}}{t} \left(\frac{degree}{nm - binding\ thickness} \right) \tag{1.13}$$

where (RIU) means refractive index unit.

The (LOD) is the minimum change that the sensor can detect in the bulk refractive index, a layer thickness or concentration. LOD is divided into bulk (LOD_B) and surface (LOD_S):

$$LOD_B = \frac{3\sigma_{SP}}{S_B} \tag{1.14}$$

$$LOD_S = \frac{3\sigma_{SP}}{S_S} \tag{1.15}$$

where σ_{SP} : is the standard deviation of measured λ_{SP}, θ_{SP}, or I_{SP} with respect to the sensor type.

Chapter 2 : Teflon AF Patterning for Surface Plasmon Sensing

2.1 Introduction

Teflon AF is a class of amorphous fluoropolymers that has unique properties such as a low dielectric constant, high optical clarity, and low refractive index. In addition, the chemical structure of Teflon AF, shown in Figure (2.1), provides it with high chemical and thermal resistance [1]. On account of these properties, Teflon AF has gained significant interest in the following applications: semiconductors, biomedical, fiber-optics, optical materials, photonics and plasmonic sensing techniques. The diversity of these applications has led to the development of several methods for Teflon AF patterning. These include reactive ion beam milling, direct electron beam lithography and UV lithography based process [17–19]. Recently, a new patent demonstrated the ability of using Teflon AF as a negative electron beam resist [20].

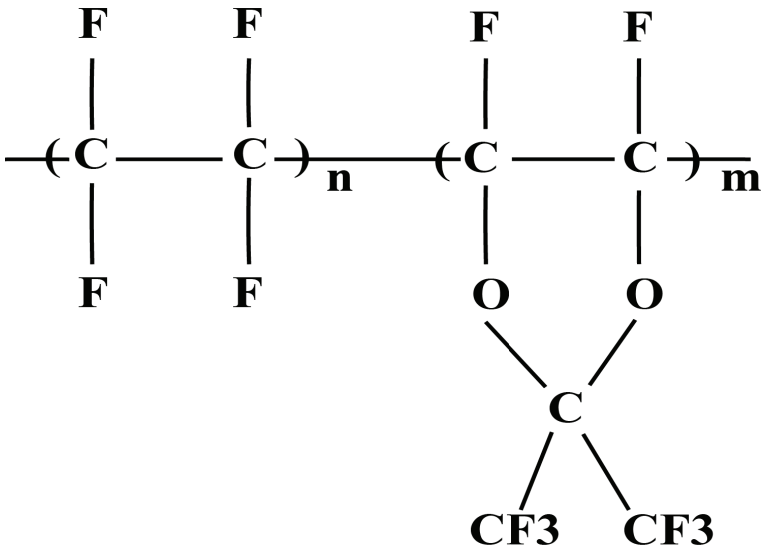

Figure 2.1: Chemical structure of Teflon AF [1].

2.2 Teflon AF patterning with variable pressure electron beam lithography (VP-EBL)

The high demand for Teflon AF patterning, the difficulty of writing a grating on gold for grating-based surface plasmon excitation, and our intention to excite the short and long range of surface plasmon resonance by grating-based configuration, all motivated us to study new ways for Teflon AF patterning. The proposed method is depicted in (Figure 2.2) below and discussed in subsequent sections.

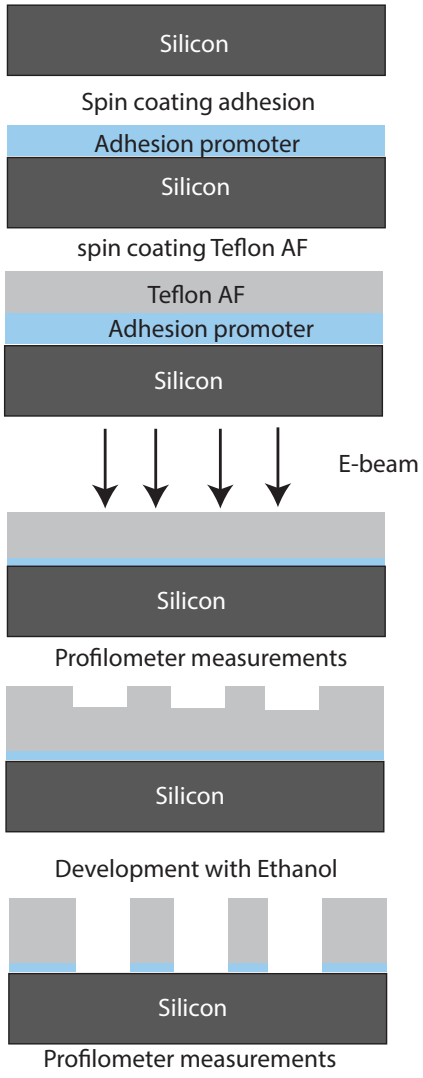

Figure 2.2: Teflon AF patterning process,

2.2.1 Sample preparation and Teflon AF thin film coating

Depending on the application, the substrate was either a microscope slide with properties similar to BK7 or silicon wafer. The BK7 substrate was used for sensor fabrication, and the silicon wafer was used for lithography study. The BK7-slide were cleaved into 1x1 square inches, and cleaned by ultrasonication in acetone, ethanol and water for 5 minutes for each solvent to remove impurities and glass particles due to the cleaving process. The Teflon AF solution has a high viscosity as purchased; therefore, it was diluted with FC-40 (3 M Inc.) to different weight ratios from 1 : 2.5 to 1 : 6 determined by the required thickness of the film. Since Teflon AF is non-adherent to the glass and silicon surfaces, it was necessary to coat the sample with an adhesion promoter layer. The adhesion promoter was prepared by mixing a fluorosilane, 1H,1H, 2H, 2H perfluorodecyltriethoxy silane (Lancaster Synthesis, Inc.), ethanol, and DI-water with weight ratio $(1 : 95 : 5)$. The adhesion layer was spun at 2000 RPM for 10 seconds, and baked at 110 °Cfor 10 minutes. The diluted Teflon AF resist were spun at 500 RPM for 10 seconds to form a uniform layer; then spun at different speeds from 1000 RPM to 6000 RPM to determine the appropriate speed for the proper thickness, and baked at 165 °C. Finally, ellipsometry was used (Ellipsometer M-200, J.A. Woollam Co. Inc.) to measure the film thickness, where the Teflon AF layer fit as a Cauchy material model. Figure (2.3) shows the speed versus thickness for each ratio of dilution (Teflon AF to FC-40), and Figure (2.4) shows the optical properties of Teflon AF film on a silicon wafer.

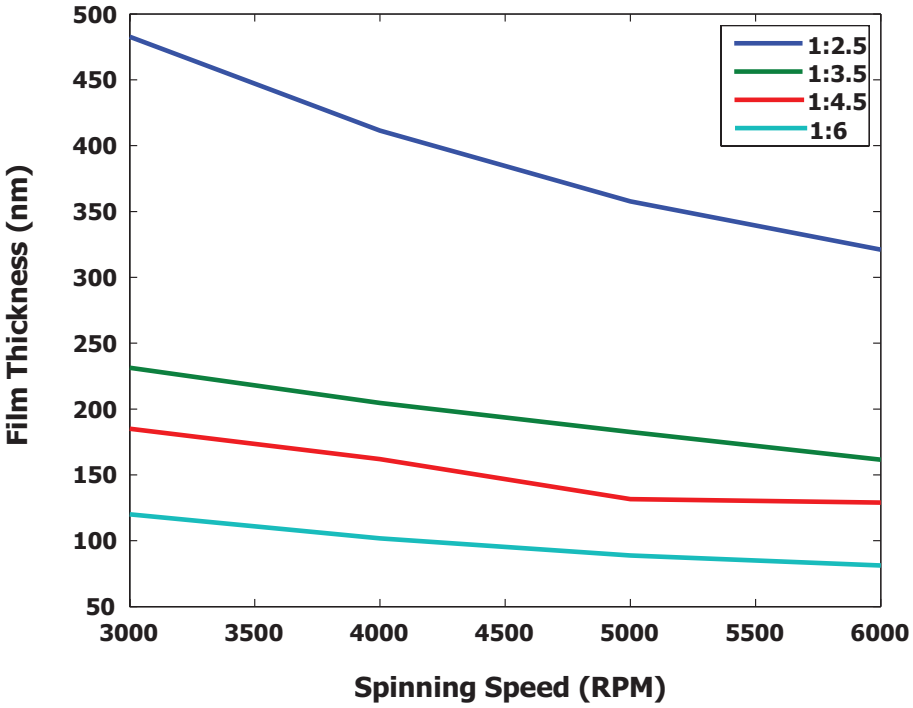

Figure 2.3: Teflon AF film thickness as function of spinning speed and dilution ratio.

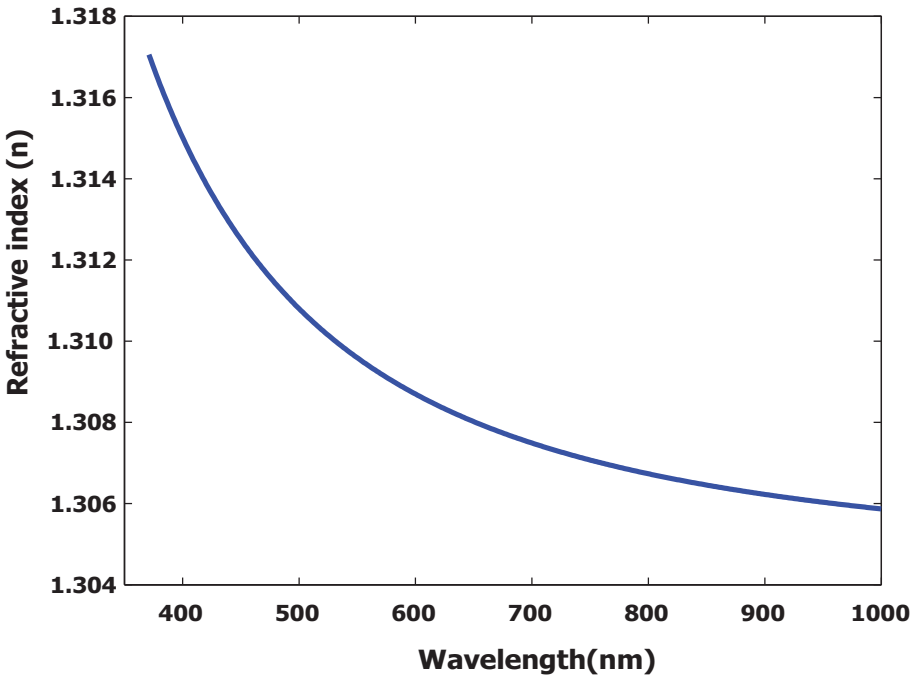

Figure 2.4: Teflon AF refractive index as function of wavelength measured by ellipsometry.

2.2.2 Lithography process

Low resolution features

In this step, we employed variable-pressure electron-beam lithography (VP-EBL), typically used to mitigate charging, for positive tone patterning of Teflon AF. This process eliminates problems associated with lifting off spin coated films, provides complete material removal (unlike direct patterning), and minimally affects the properties of the undeveloped Teflon (unlike negative tone processes). Rectangles $(25\mu m \times 100\mu m)$ were exposed in spin-coated Teflon AF films (480-nm thick) using beam energies of 10, 20, and 30 keV. Exposures were conducted under either high vacuum ($\sim 5 \times 10^{-5}$ Torr) or 1 Torr of water vapor in a FEI environmental scanning electron microscope (ESEM) with a Raith ELPHY Plus pattern generator. Samples were developed for 120 seconds in ethanol, and a profilometer was used to measure the pattern depth before and after development.

Plots of pattern depth vs. dose in Figure (2.5) confirm that a significant relief pattern is present before development for both high-vacuum and 1 Torr H_2O exposures. However, water vapor does not appear to accelerate pattern formation through e-beam induced etching. For high-vacuum exposures, development revealed both positive and negative tone behavior at lower and higher doses respectively; however, the pattern failed to clear under all conditions. For exposure in water vapor, positive tone behavior was observed with full clearance. This dramatic difference may be associated with radiation induced reactions involving water, as the radiation degradation of Teflon depends strongly on the ambient environment [21].

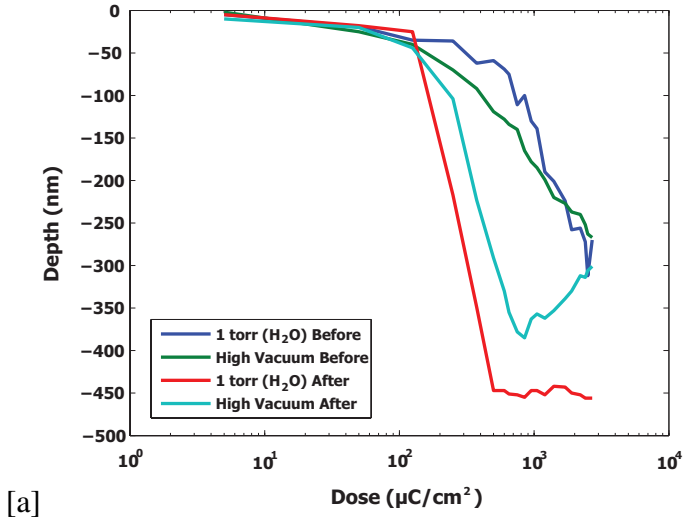

[a]

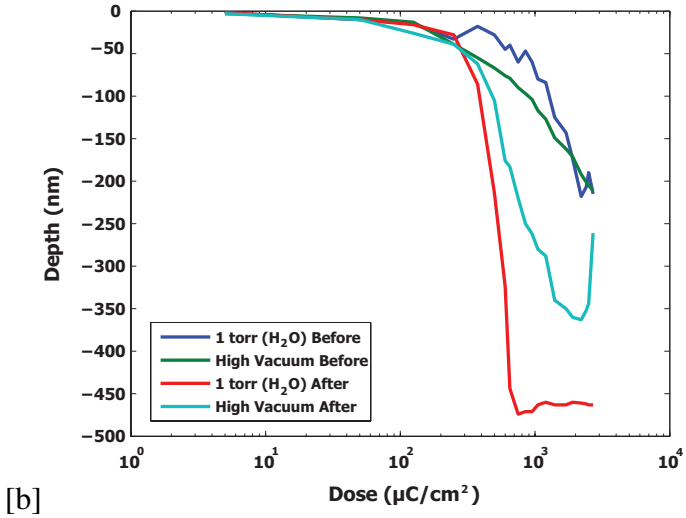

[b]

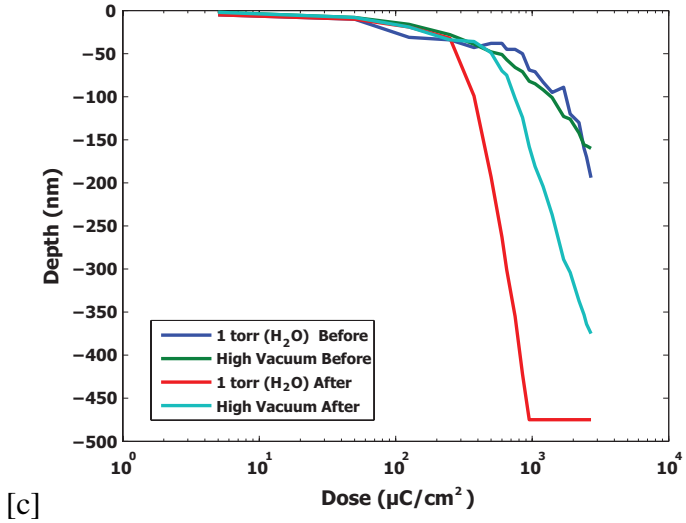

[c]

Figure 2.5: Dose vs. Depth for e-beam exposure of Teflon AF using [a] 10 keV, [b] 20 keV, and [c] 30 keV beam energies under high-vacuum and 1 Torr water vapor conditions before and after development.

Depths were measured both before and after development in ethanol as noted in the legends. High vacuum exposures exhibited both positive and negative tone behavior but failed to clear (note minima near 900 and 2000 $\mu C/cm^2$ at 10 and 20 keV respectively). However, exposure under water vapor yielded positive tone behavior and clearing doses from 500 to 1000 $\mu C/cm^2$. The threshold dose and contrast was estimated by using Figure (2.6) and equation (2.1).

$$\gamma = \left[\log\left(\frac{D_{100}}{D_0}\right)\right]^{-1} \tag{2.1}$$

Where D_0 is the the threshold dose for resist removal, D_{100} is the dose for complete resist removal, and Figure (2.6) shows how they were calculated. Estimated contrasts were 1.5, 2.9, and 2.0 for 10, 20, and 30 keV respectively.

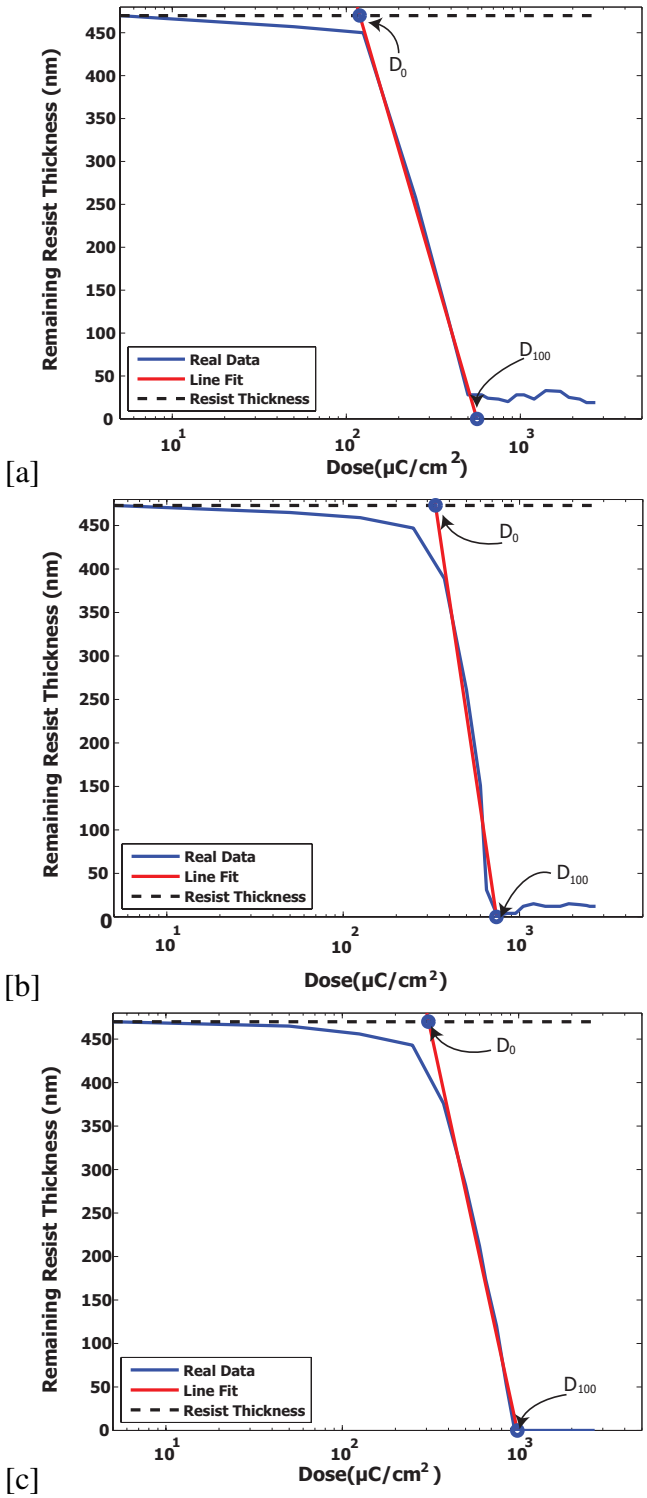

Figure 2.6: Threshold and contrast estimation plot for 1 Torr water vapor condition after development [a] 10 keV, [b] 20 keV, and [c] 30 keV.

High resolution features

For using Teflon AF as a resist, we explored the highest resolution that can be achieved with thinner films. Different sets of nested lines were exposed into an 80 nm film under 1 Torr pressure and beam energies of 10 keV, 20 keV, and 30 keV. The exposed nested lines were: 15 nm to 500 nm half-pitch with doses ranging from 2,000 to 14,600 pC/cm and step size of 24 nm. After exposure and development for 120 second with ethanol, the sample was coated with a thin gold layer (around 8 nm) to mitigate charging and protect the sample from etching during the imaging. SEM imaging of the structures revealed pithes approximately 1.5 times larger than the desired size. This implies that the writing field is larger by the same ratio and the dose is lower by the same factor. The smallest half-pitch observed on the sample was 75 nm. Figures (2.7 - 2.10) show the high resolution structures with the exact dimensions and doses.

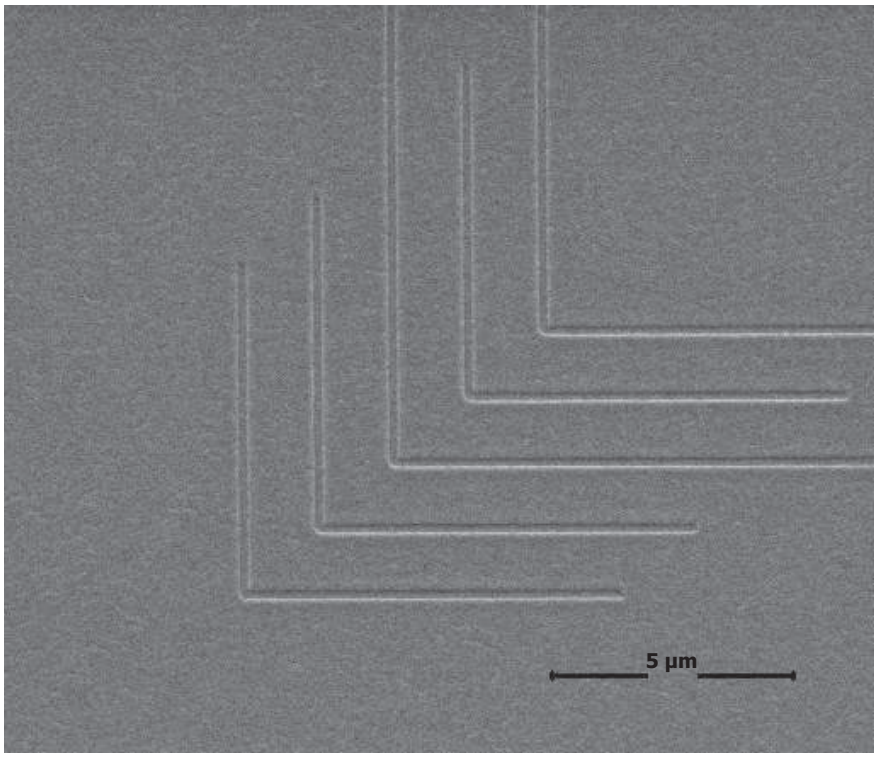

Figure 2.7: Nested lines with 750 nm half-pitch, exposed with a beam energy of 10 keV and a dose of $1,300$ pC/cm with 1 Torr H_2O pressure.

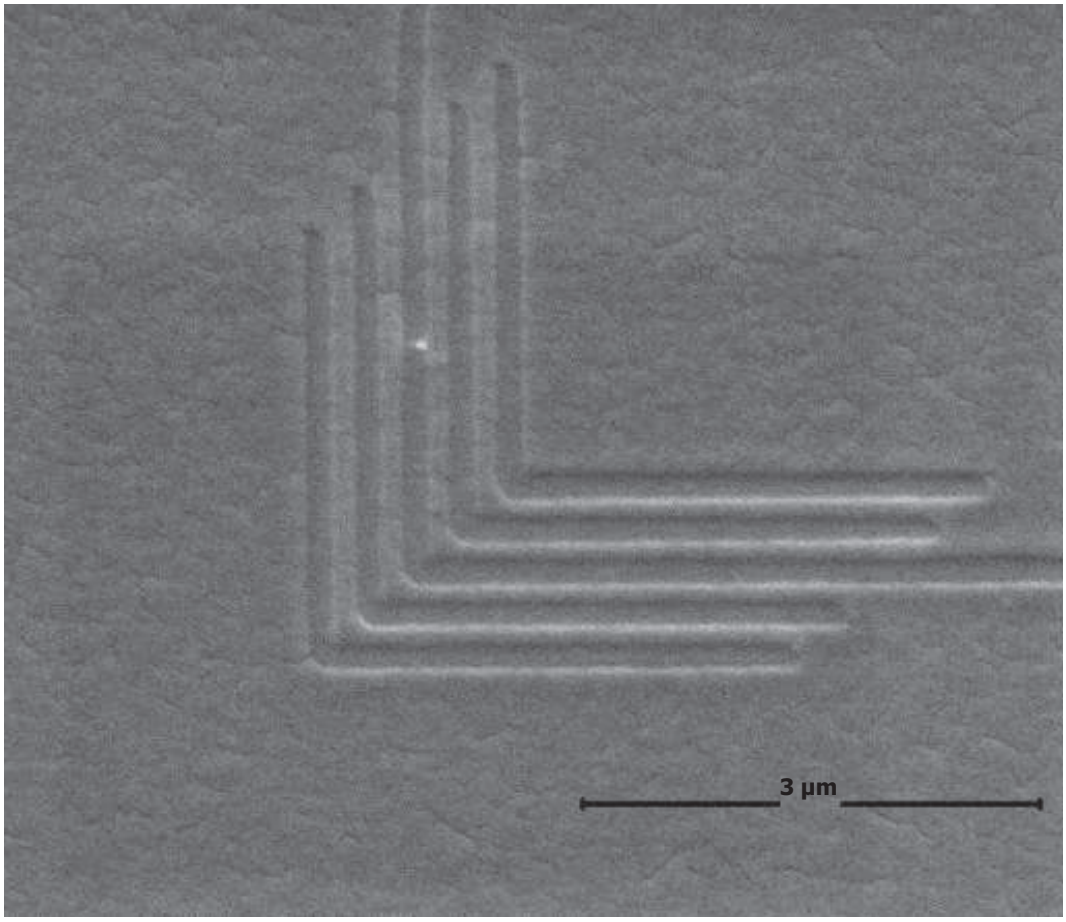

Figure 2.8: Nested lines with 150 nm half-pitch, exposed with beam energy of 10 keV and a dose of $5,200\ pC/cm$ with 1 Torr H_2O pressure.

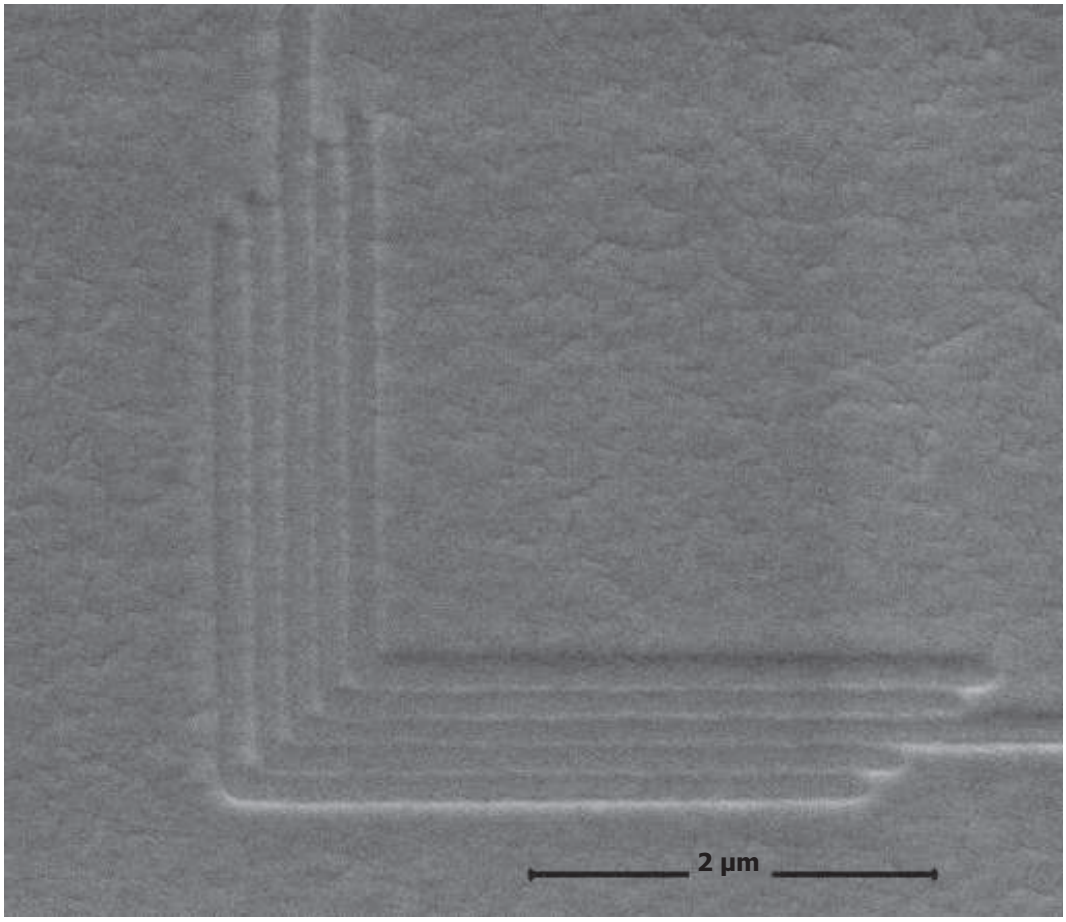

Figure 2.9: Nested lines with 75 nm half-pitch, exposed with beam energy 10 keV and a dose of $5,200\ pC/cm$ with 1 Torr H_2O pressure.

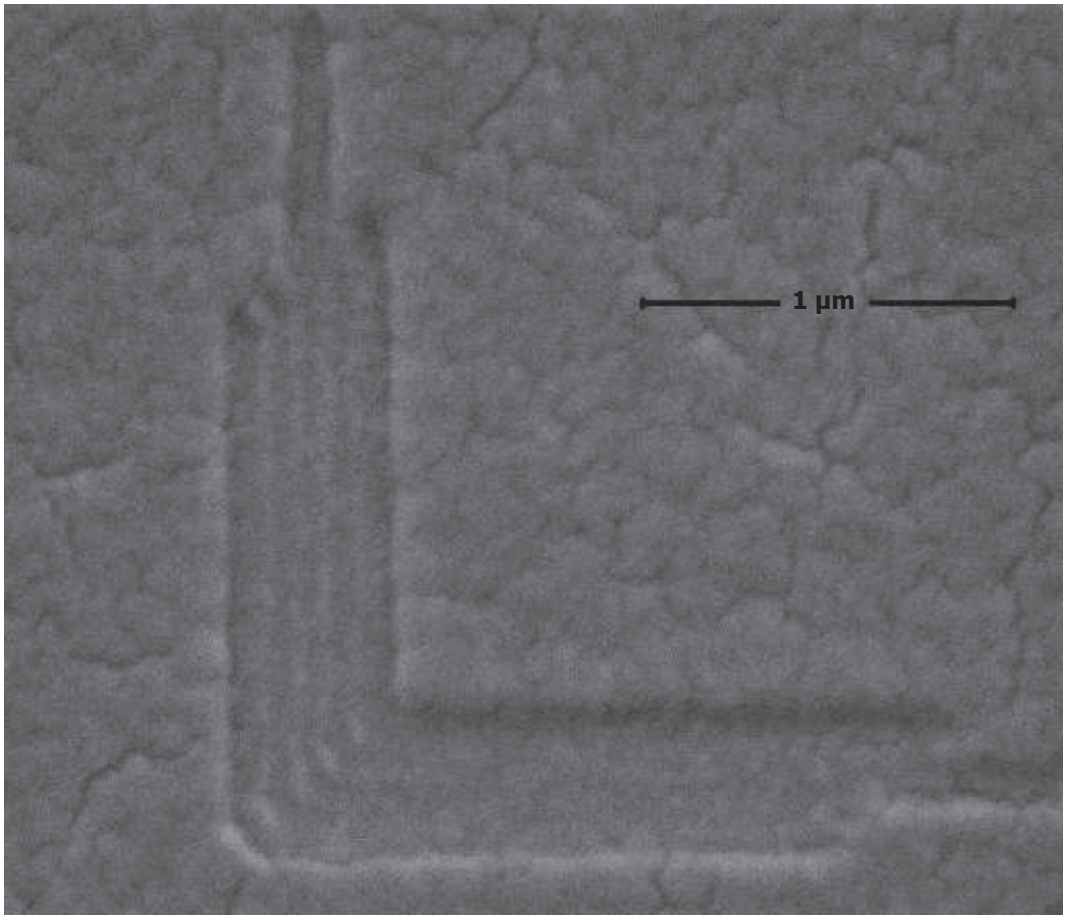

Figure 2.10: Nested lines with 38 nm half-pitch, exposed with beam energy 10 keV and a dose of $1,300\ pC/cm$ with 1 Torr H_2O pressure.

Chapter 3 : Sensor Design and Fabrication.

3.1 Simulation tools

Chapter 1 provided a brief overview of dual mode SPR excitation using a dielectric grating coated with a metal layer. Chapter 2 discussed the protocol developed in our lab for fabricating gratings for SPR sensing applications. This chapter examines the various simulation tools used to study the response of grating based SPR sensors. Three simulation tools were tested [22–24]. These tools all depend on rigorous coupled wave theory (RCWT) to solve multilayered structures, but each one has a different algorithm. RCWT is a precise solution for Maxwell's equations for an incident wave on multilayered structures, where the electromagnetic fields are expressed by Fourier series [25]. The accuracy of RCWT is determined by the number of orders that were used for field and material properties. Dual mode grating based SPR sensor simulations with these tools was challenging due to different reasons for each tool. The next sections discuss each tool and its respective advantages and disadvantages.

3.1.1 OptiScan

OptiScan is a matlab based graphical user interface (GUI) simulation tool, developed by the Milster group at Arizona University [22]. This tool is used for 2D optical system simulations and it has a wide range of applications. One of its accessories is the RCWT calculator, which we used for a sensor design test. Keathley and Hastings utilized this code for nano-gap enhanced SPR sensors, and it revealed reliable matching between the simulation and test results [26]. OptiScan is characterized by a user friendly interface and user prescribed material properties, where the user can use the required material properties as tabulated data for wavelength (in μm), real part of refractive index and imaginary part of refractive index. However, this code was not efficient with longer period and multilayer structures, and the calculation time increased as the grating period increased. In addition, if the structure contains metals, it requires twice the minimum number of order (N). The minimum number of order is define as:

$$N = 2\Lambda/\lambda$$

Where Λ is the grating period and λ is the incident wavelength. Further simulations have been carried out with the RCWT calculator; code did not converge quickly and there was a deviation between the order number and code convergence. The design in Figure (3.1) was tested with the RCWT calcualtor in OptiScan, and it was discovered that increasing the order number did not improve the accuracy of the calculation. Results of the diffraction efficiency for the the design are shown in Figure (3.2).

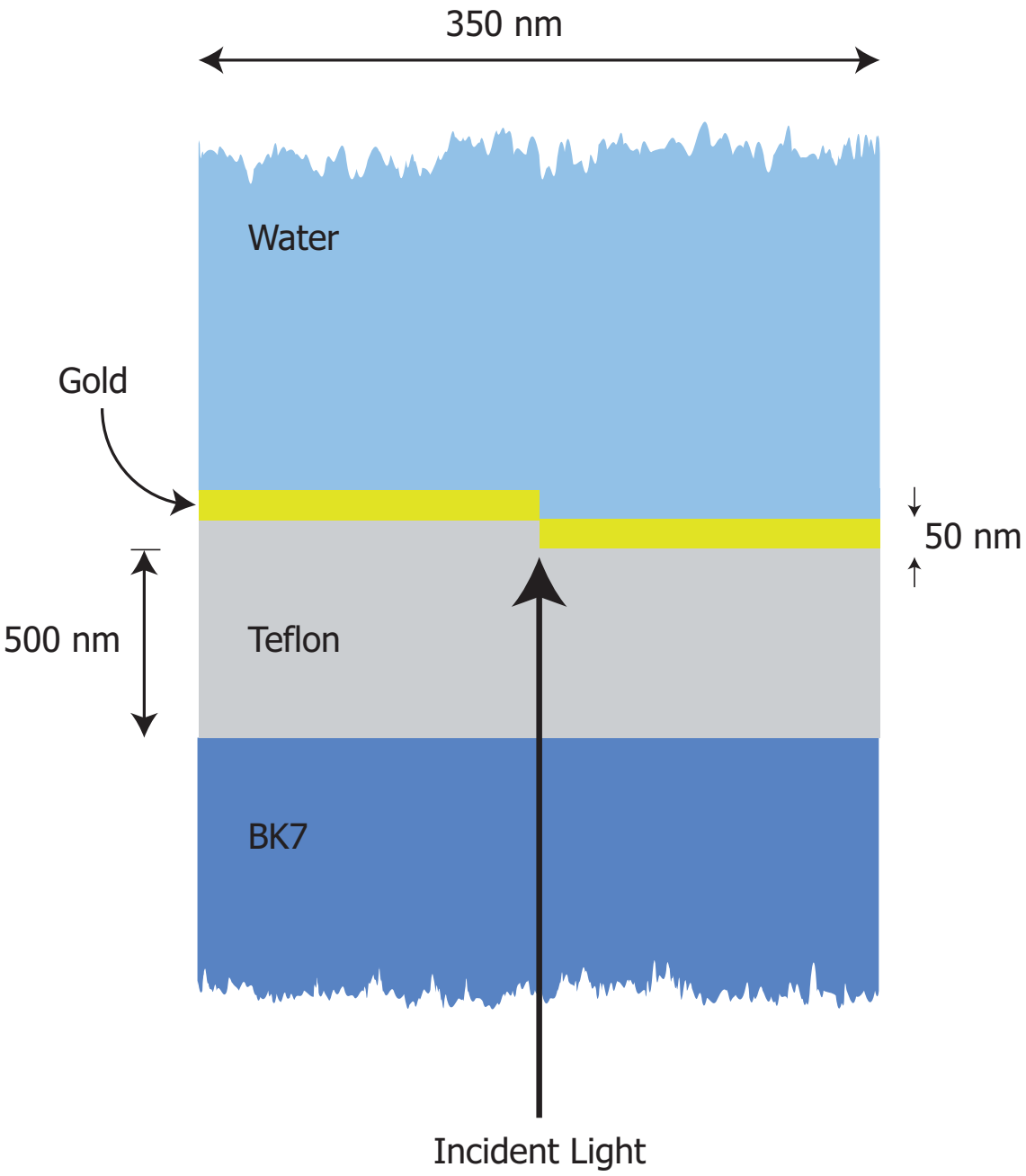

Figure 3.1: Design tested with OptiScan.

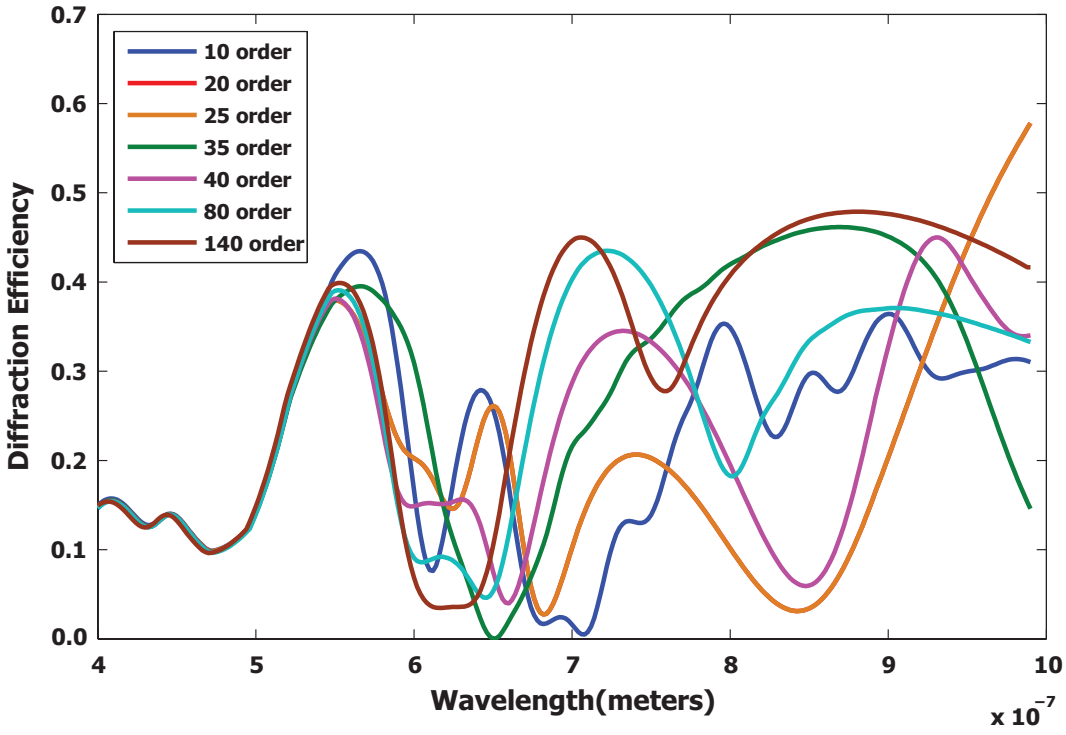

Figure 3.2: Diffraction efficiency as a function of wavelength and number or orders for the grating structure in Figure (3.1).

3.1.2 S4: Stanford stratified structure solver

S4 is another simulation tool used to implement RCWT calculations for 2D and 3D structures based on C/C++ language [23]. The code was published in 2012 and first released on the nanohub website for Purdue University in April 2013. The online version has two programing methods: a graphical user interface or script writing. The GUI is limited to certain materials, therefore, we used the script writing method, where we can specify the desired material properties. The paper disclosed that S4 is not efficient with metal gratings, we used the code anticipating that this limitation had been addressed in newer versions, the latest version have been published in August 2014. Unfortunately, the code did not work well with metal-dielectric gratings, and the solution did not converge as we increased the number of orders. The design used for testing this code is illustrated in Figure (3.1).

A different number of orders were tested for the same design, and the resulting curve for reflectance is shown in Figure (3.3). The code written for this design is given in detail in Appendix A.

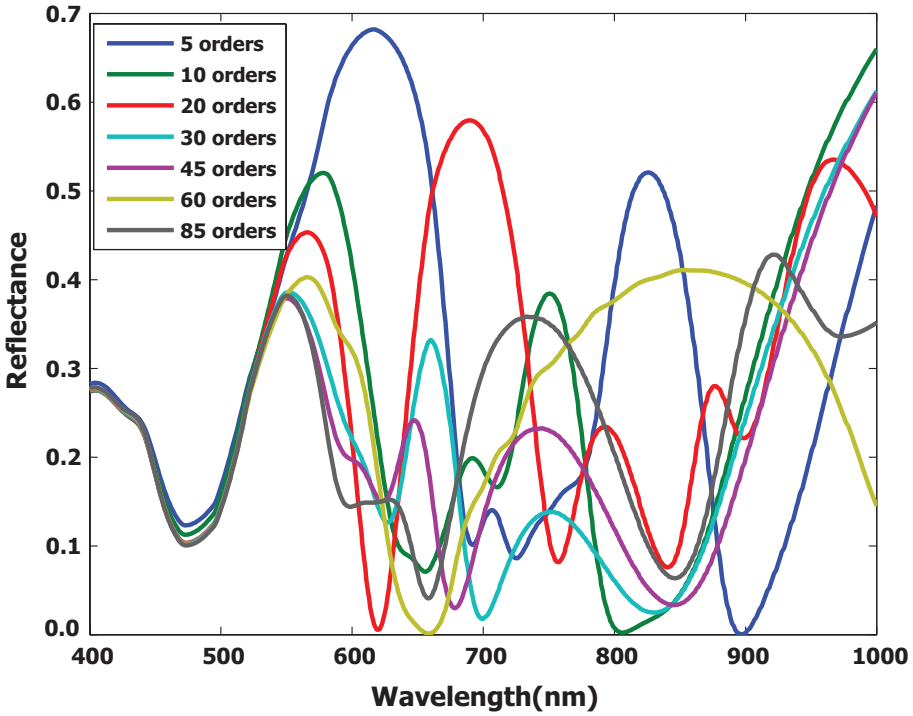

Figure 3.3: Reflectance as a function of wavelength and number of orders for the grating structure in Figure (3.1) tested with the S4 tool from the nanohub website.

,

3.1.3 PhotonicsSHA 2D

PhotnonicsSHA 2D is a spatial harmonic analysis code developed by Xingjie Ni *et al.*, and released online on the nanohub website [24]. The code solver was written in C with a linear algebraic package (LAPACK). The GUI was written with Qt and Qwt libraries. This tool has a user friendly GUI, and it is very useful for 2D multilayer grating simulation. The design in Figure (3.1) was tested with photonicsSHA 2D and the results obtained showed better convergence than the previous two tools. However, this tool does not allow for the addition and use of materials outside of its limited database, which proved to be major disadvantage for our sensor design. Therefore, for the design shown in Figure 3.1, water was used instead of Teflon AF and the simulation wavelength range was limited to 826 nm because the database does not include water dielectric constant values above that wavelength. The results of the tested design are depicted in Figure (3.4), which shows a consistent profile of the reflectance and better convergence with higher order numbers. This tool was selected for our design simulation and testing.

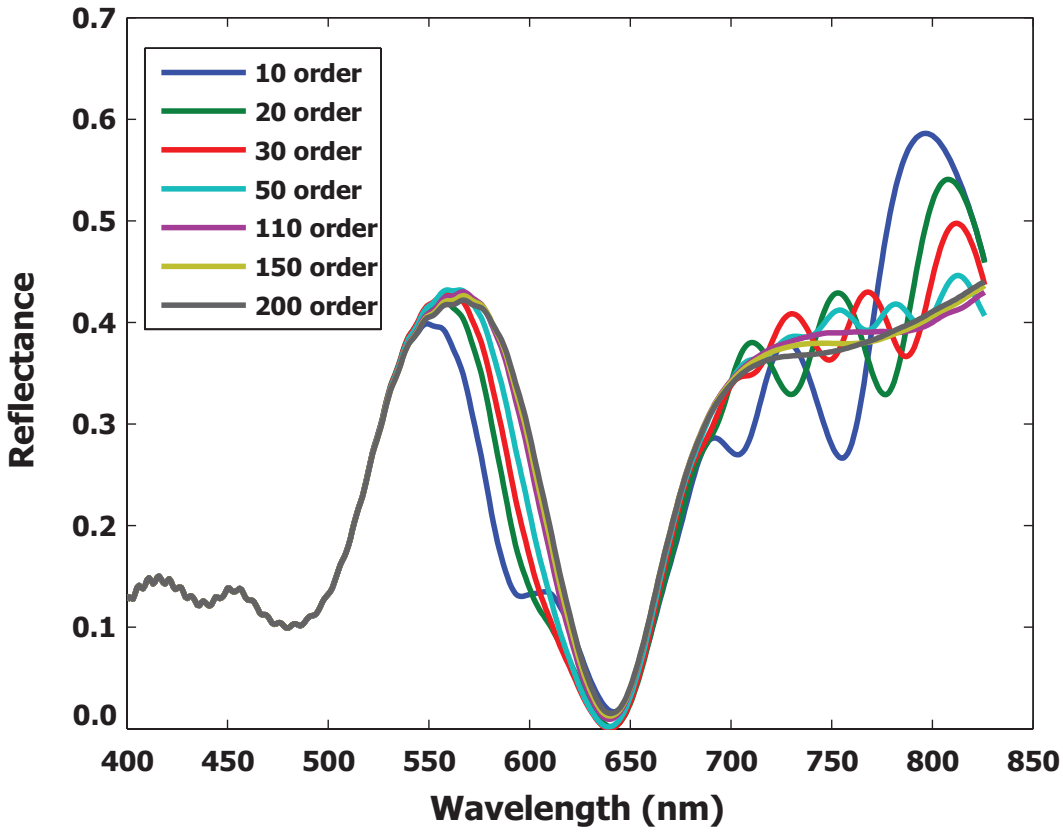

Figure 3.4: Diffraction efficiency as a function of wavelength and number of orders for the grating structure in Figure (3.1) tested with PhotonicsSHA 2D.

3.2 Sensor chip design and fabrication

After testing the simulation tools above, it was necessary to find a grating design that supports a dual mode surface plasmon. Starting with equation (1.10), matlab code was developed for the dispersion relation in Figure (1.12). Results show that it is possible to excite LRSP and SRSP by a grating design made from the available materials. The simulation was done for different grating periods as shown in Figure (3.5). The fabrication process for the sensor follows the process in section 2.2, where the substrate is a BK7 microscope slide. The Teflon AF was spun to a thickness of 550 nm (measured by ellipsometry, M-200, J.A. Woollam Co. Inc). Since the proximity effect and etching profile for Teflon AF was

unknown, sets of single pixel lines and rectangles with different geometry were exposed on the sample to identify which geometry will be useful for surface plasmon excitation. The rectangles and line length is 200 μm. The exposure conditions are tabulated in table (3.1). After etching, the sample was developed with ethanol for 120 seconds and coated with a thin gold film by RF deposition. The gold thickness was 46 nm.

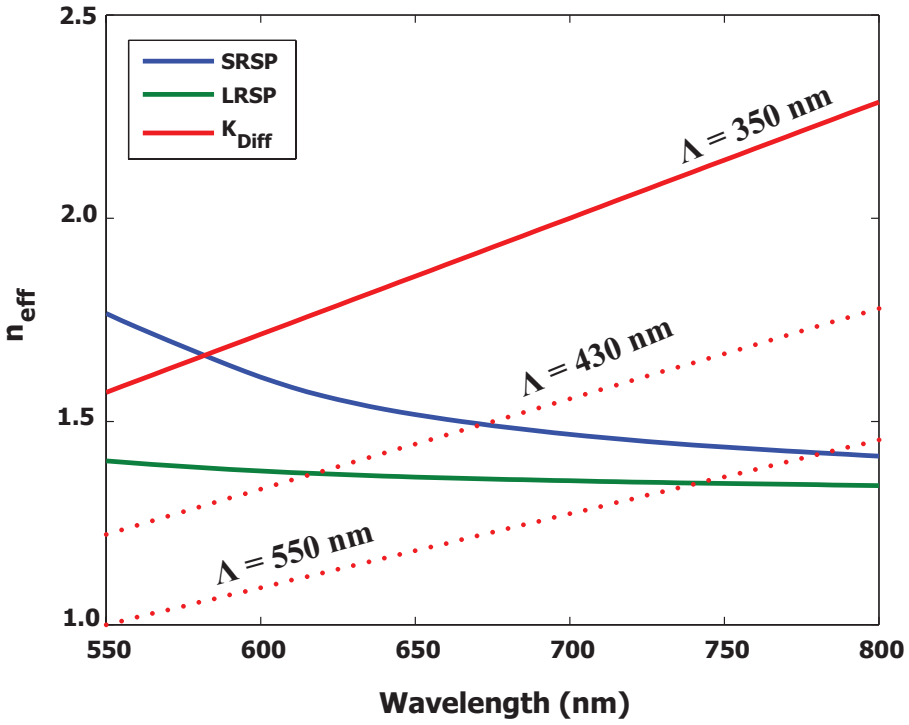

Figure 3.5: Grating period test for dual mode excitation with grating structure.

Table 3.1: Exposure conditions for sensor fabrication.

Parameter \ Width	305 nm	365 nm	Single pixel	Single pixel
Pitch (nm)	730	855	305	430
Beam energy (keV)	30			
Beam current (nA)	172			
Area dose (μC/cm^2)	135	135	-	-
	335	335	-	-
Line dose (pC/cm)	-	-	8200	8200
	-	-	6560	6560
	-	-	9835	9835
H_2O pressure (Torr)	1			
Step size (nm)	20			

Chapter 4 : Results and Discussion

4.1 Experimental setup

Chapter three provided a detailed description for the sensor chip fabrication and simulation tools. In order to test the chip, The experimental setup consisted of a microscope (Carl Zeiss:Axiovert 405 M) and a spectrometer (Ocean optics HR4000CG-UV-NIR) with Spectrasuite software package, was used to analyze the sample spectrum as shown in Figure (4.1). The etched patterns were on a 200 square micrometers area; therefore, it was necessary to use a microscope to adjust the incident light on the patterned area. The sample was mounted to the microscope stage and the light was normally incident on the sample. The aperture was used to control the illumination field to obtain reflected light from only the zero order of the patterned area. As mentioned previously in chapter one, the excitation of surface plasmons occurs with transverse magnetic waves. Thus, a polarizer was used to filter the reflected light from the sample either as transverse electric (TE) or transverse magnetic (TM) polarized waves. In addition, a silver coated mirror was used as for reference spectrum.

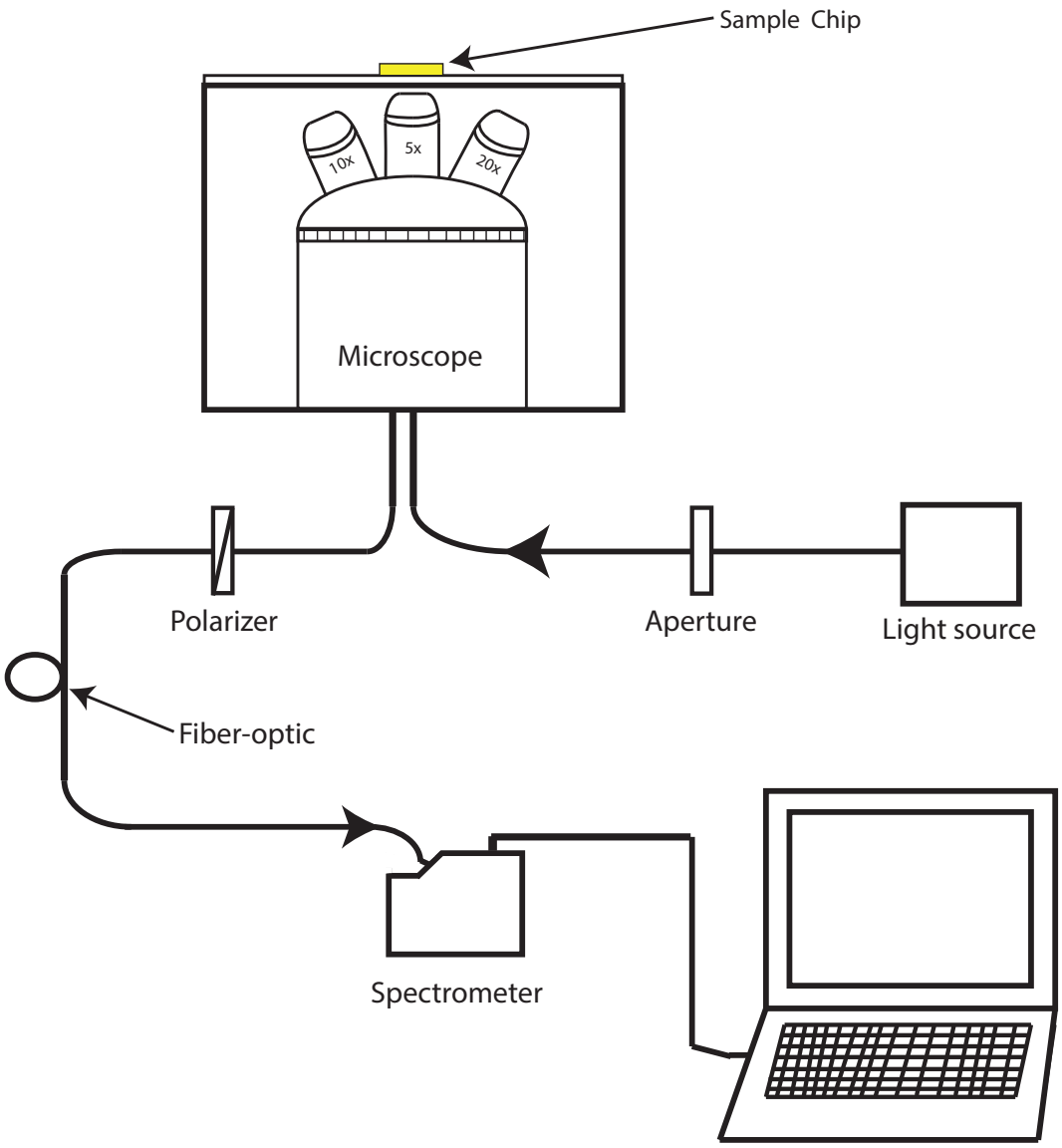

Figure 4.1: Experimental setup for sensor chip testing.

4.2 Experimental results

The experimental setup in the previous section was used to analyze the spectrum of the sensor chip. TM wave reflectivity was measured for all of the patterns to identify which one supports the SPR excitation within the wavelength range that the spectrometer can detect. It was found that the grating etched with single pixel lines with a 430 nm pitch supported SPR excitation. The SEM image for the grating is depicted in Figure (4.2).

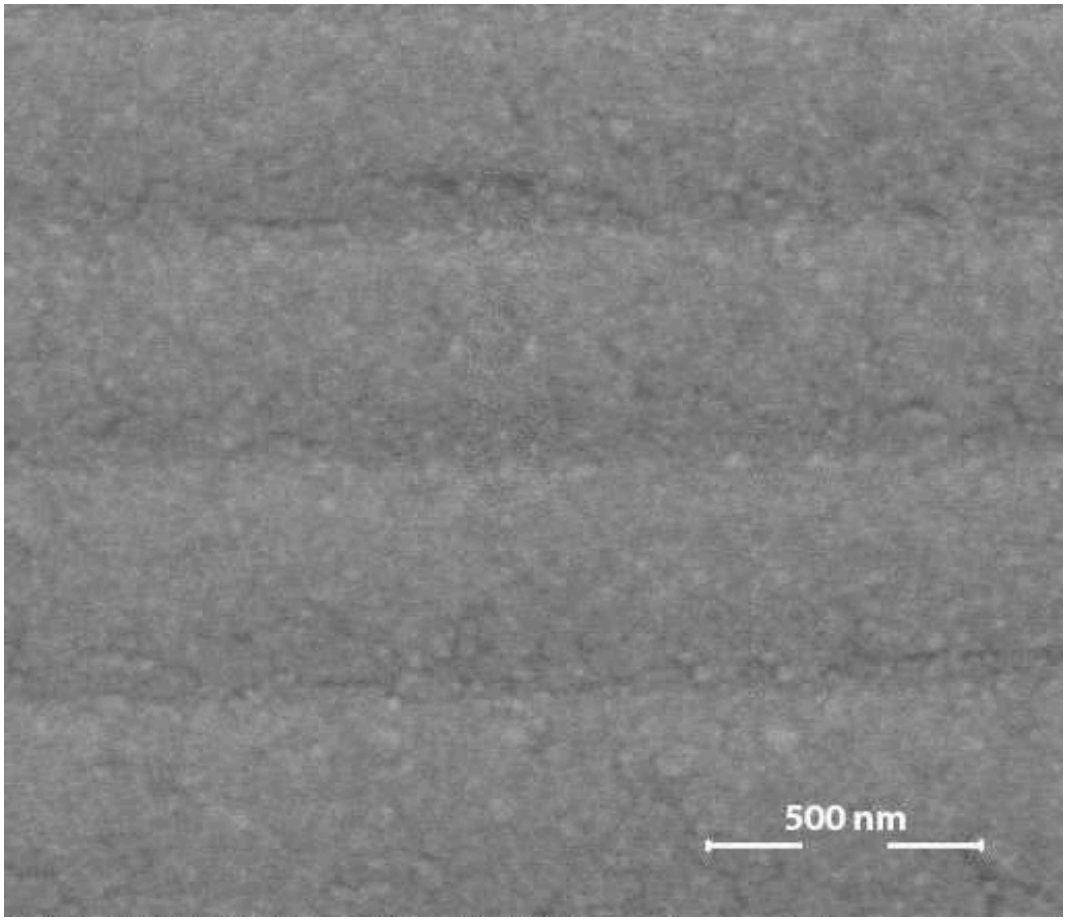

Figure 4.2: SEM image for a grating structure that supports dual surface plasmons excitation. The grating period is 430 nm. The image was taken after the optical measurements due to carbon deposition and etching of the Teflon with high beam energies.

More accurate measurements were performed to get the exact spectrum for the grating for TE and TM modes without water on top of the grating (top dielectric layer). The experiment was done as follows: first, the dark spectrum was captured when the light source was off at 2 seconds scanning time, second, a reference spectrum was taken on a silver coated mirror, finally, a reflectivity spectrum was obtained from small area of the grating. Since we have one metal-dielectric interface, one mode was excited. The sample spectrum is presented in Figure(4.3).

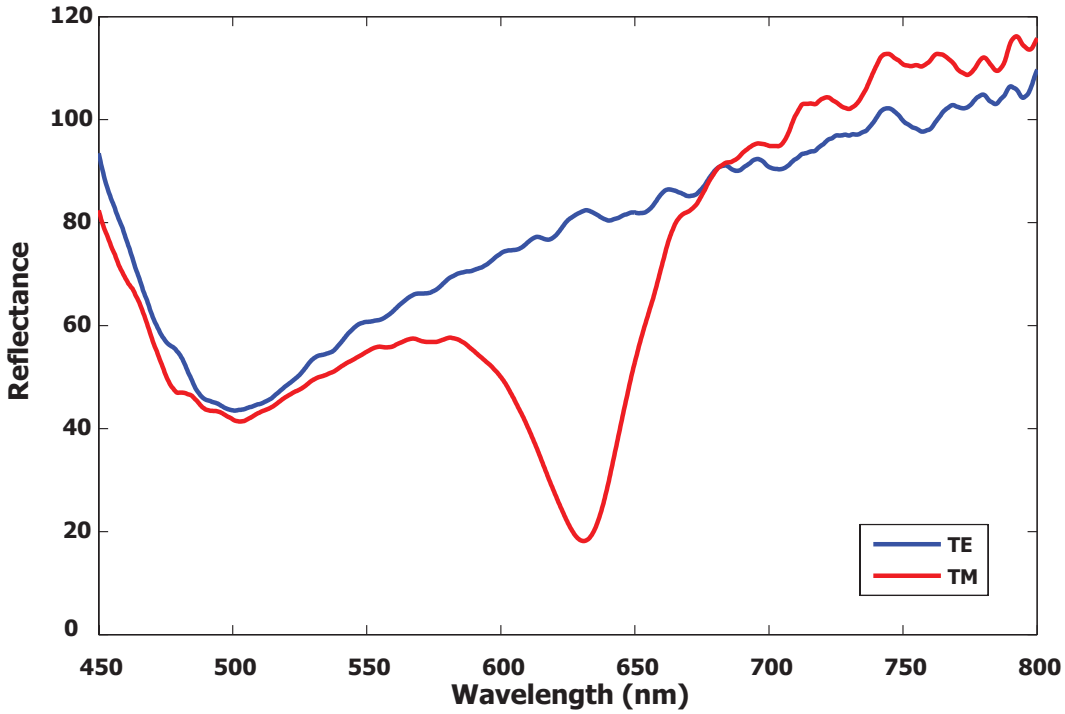

Figure 4.3: Experimental results for reflectance as a function of wavelength for TE and TM modes for the grating shown in Figure(4.2). The TM mode shows single mode excitation for SPR around 630 nm.

The experiment was repeated with water on top of the grating and SRSP and LRSP were excited as shown in Figure(4.4).

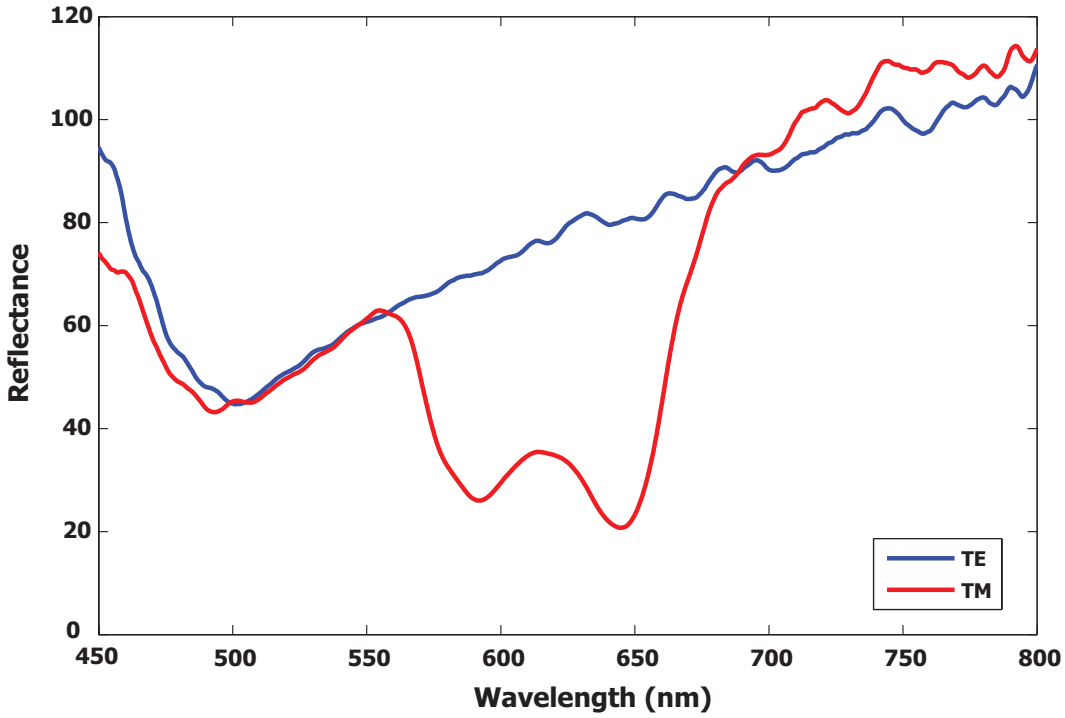

Figure 4.4: Experimental results for reflectance as a function of wavelength for TE and TM modes for the grating shown in Figure(4.2). The TM mode shows SRSP and LRSP excitation at 590 nm and 645 nm, respectively.

4.3 Simulation results

Since the etching profile and proximity effects were unknown, several simulations were carried out to understand and analyze the resulting spectra. First, we used the matlab code to calculate the dispersion relation (effective index vs. wavelength) for the surface plasmon modes and it shows a perfect match between the experimental (Figures(4.3 ,4.4)) and simulated results as shown in Figure (4.5). where the resonance wavelength can be found from the intersection of K_{diff} with SRSP and LRSP indexes. It can be seen that resonance wavelengths are 625 nm, 594 nm, and 653 nm for single mode, SRSP, and LRSP, respectively.

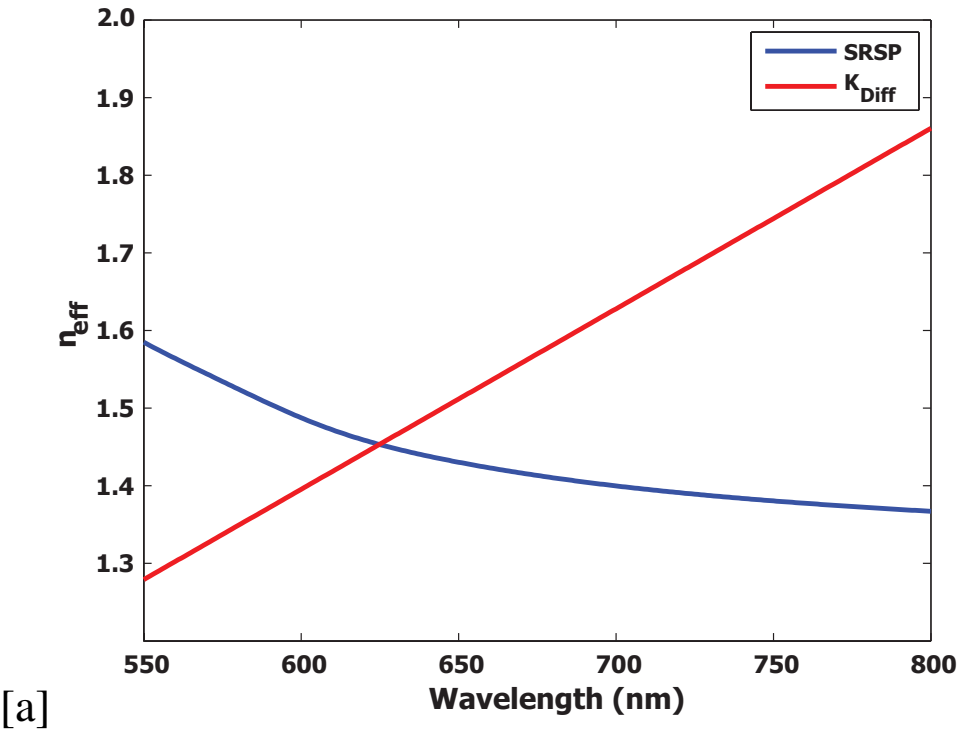

[a]

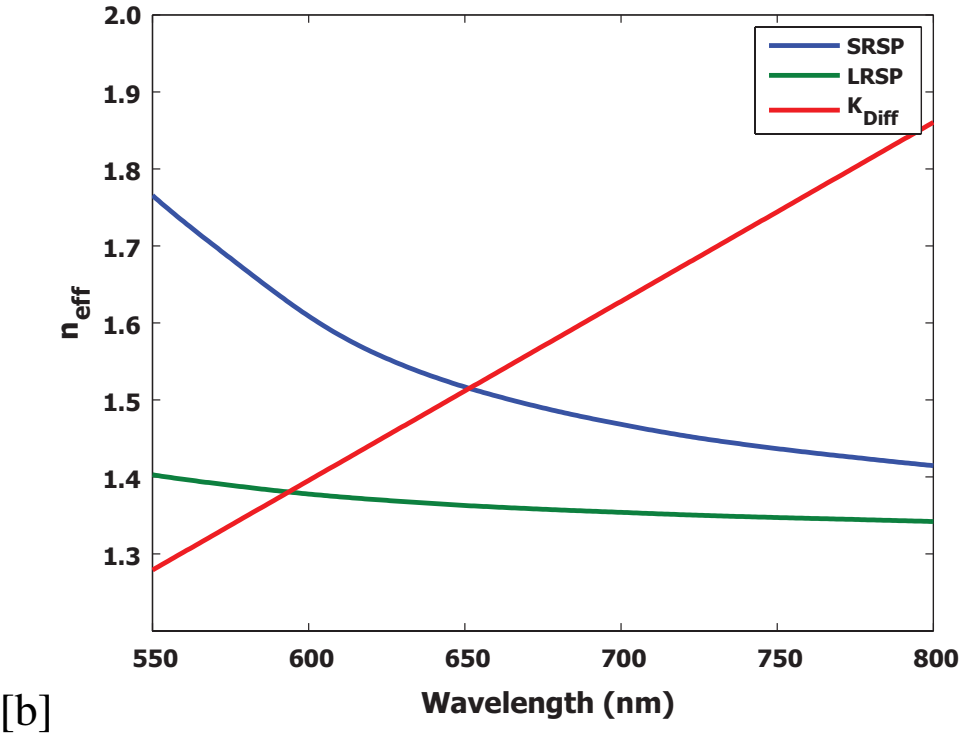

[b]

Figure 4.5: Dispersion relation for surface plasmon excitation [a] Single mode, [b] Dual mode.

Second, PhotonicsSHA 2D was used to simulate the grating structure mentioned previously. The simulated design is shown in Figure(4.6) where the depth of the etched area set to be 51 nm and the top layer set to be either air or water. The reflectance spectrum was simulated for TE and TM modes.

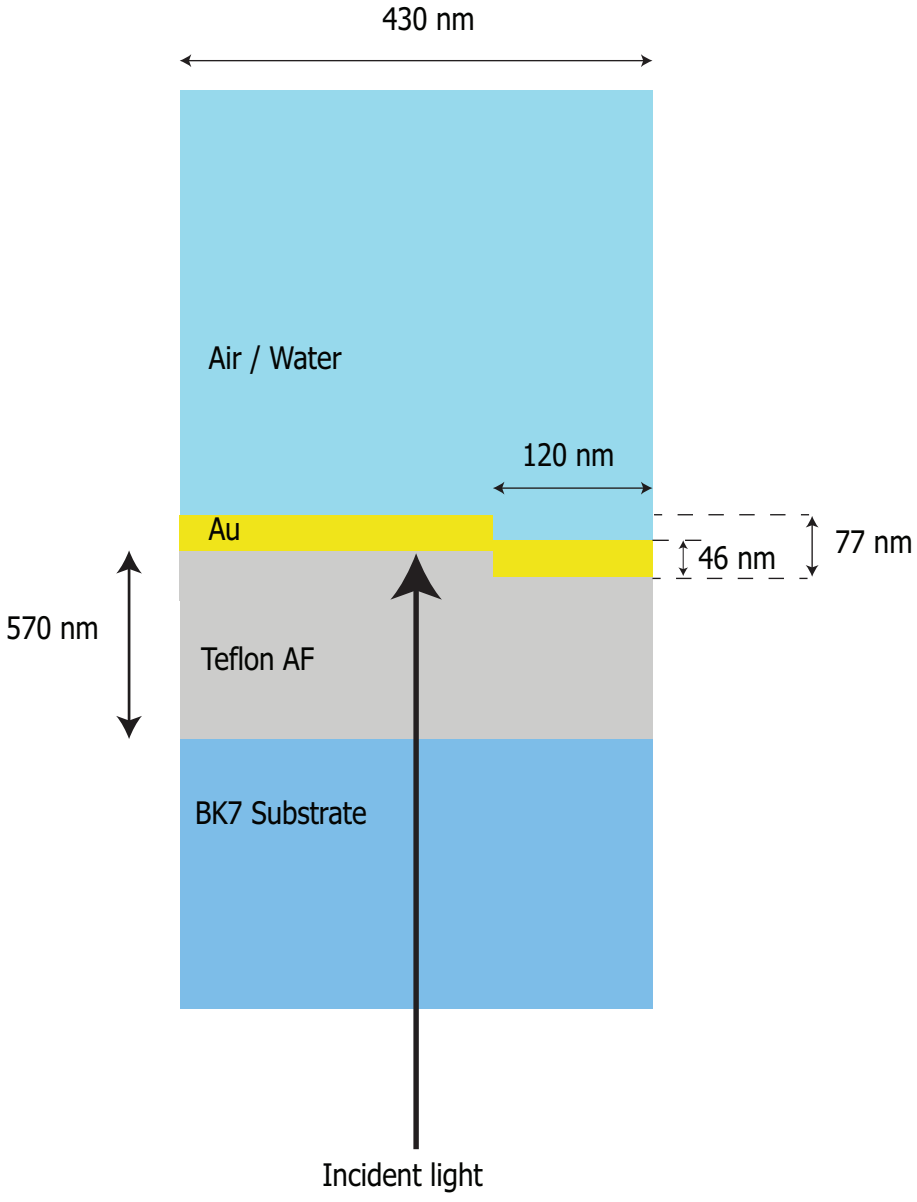

Figure 4.6: Approximate design for the grating structure in Figure (4.2) was used for simulation with PhotonicsSHA 2D.

The resulting reflectance spectrum had a shift with the resonance wavelength for both single and dual mode excitation. For comparison between experimental and simulated results, the ratio of TM to TE mode was taken, as shown in Figure (4.7).

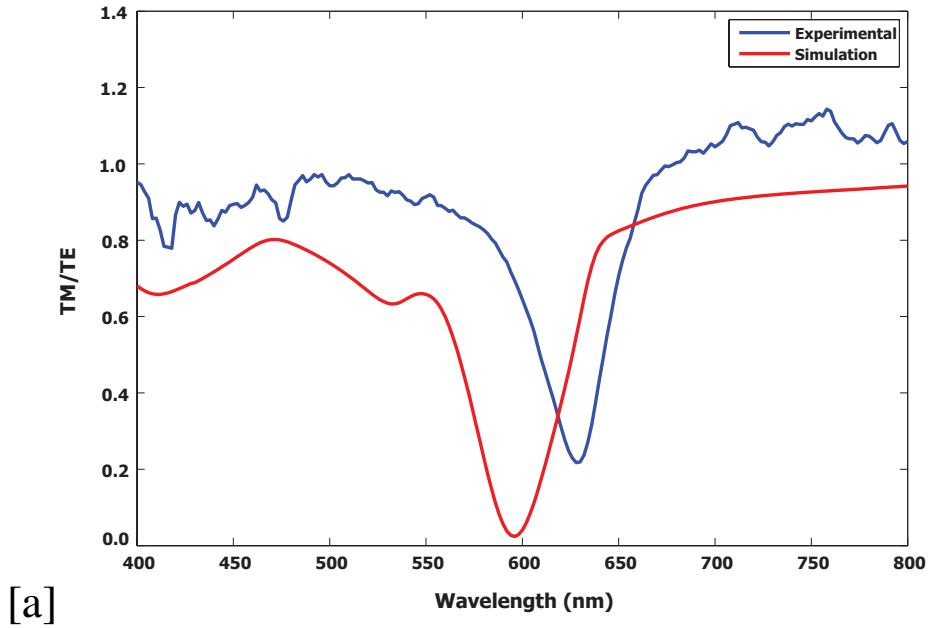

[a]

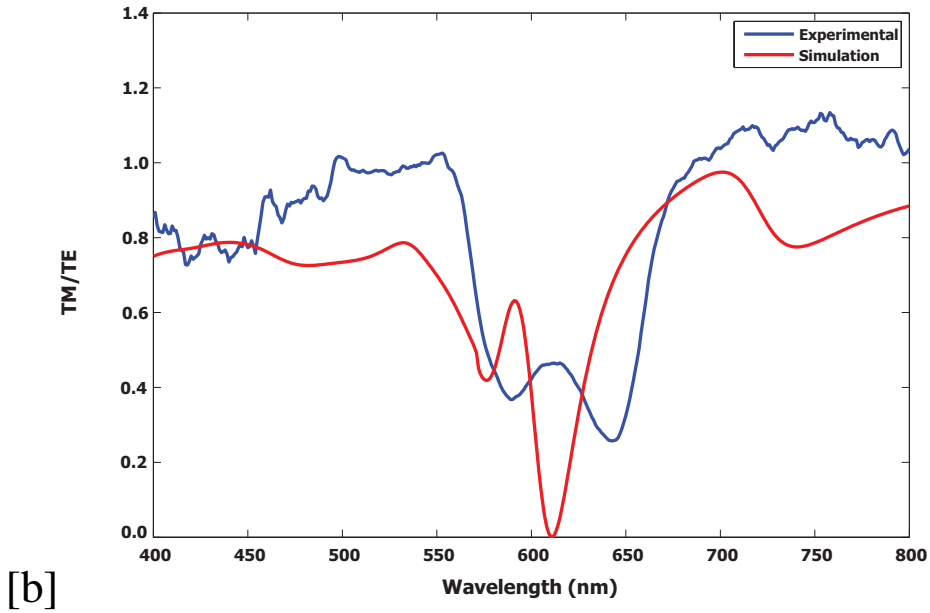

[b]

Figure 4.7: TM to TE ratio as function of wavelength for experimental and simulation results [a] Single mode, [b] Dual mode.

4.4 Discussion

The results clearly show that there is a shift in the resonance wavelength between the experimental and simulated spectra. Several reasons could account for this discrepancy. First, in the simulation with PhotonicsSHA 2D water was used instead of Telfon AF because the database does not contain optical properties for Teflon AF. Although the optical properties are similar, they are not equal. Figure (4.8) shows the refractive index for water and Teflon AF as function of wavelength.

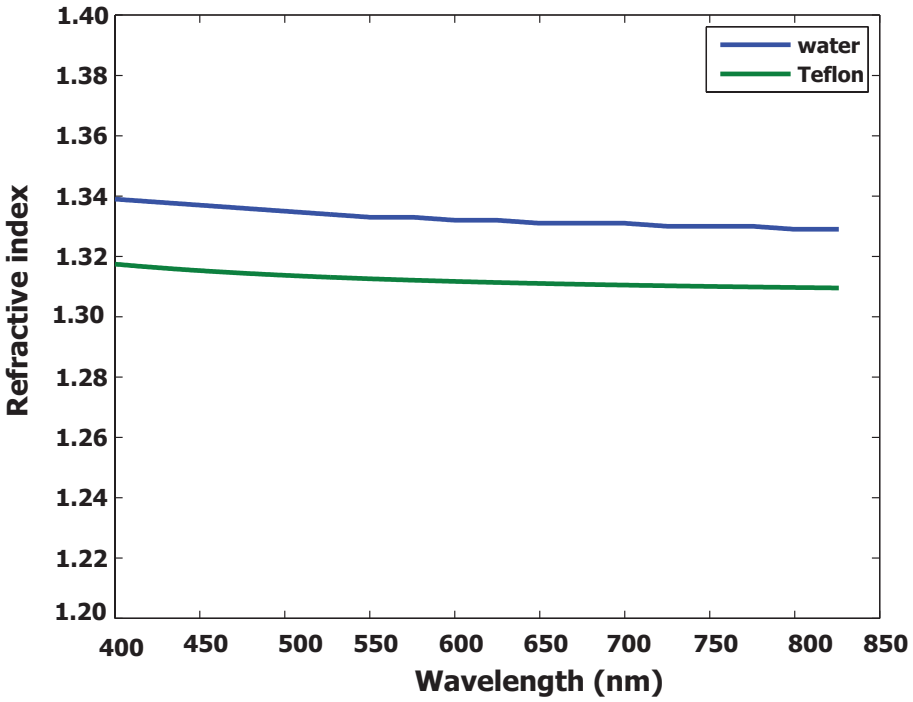

Figure 4.8: Refractive index for water and Teflon as function of wavelength.

Second, the depth and shape of the grating are unknown; we know the period of the grating only. Right edges were used to represent the trench of the grating (Figure (4.6)) while it looks like rounded edges in the real image for the grating (Figure (4.2)). Further simulations were done with different grating trench depth, and it was discovered that the depth of grating shifts the resonance wavelength and change the reflectance profile as shown in Figure (4.9).

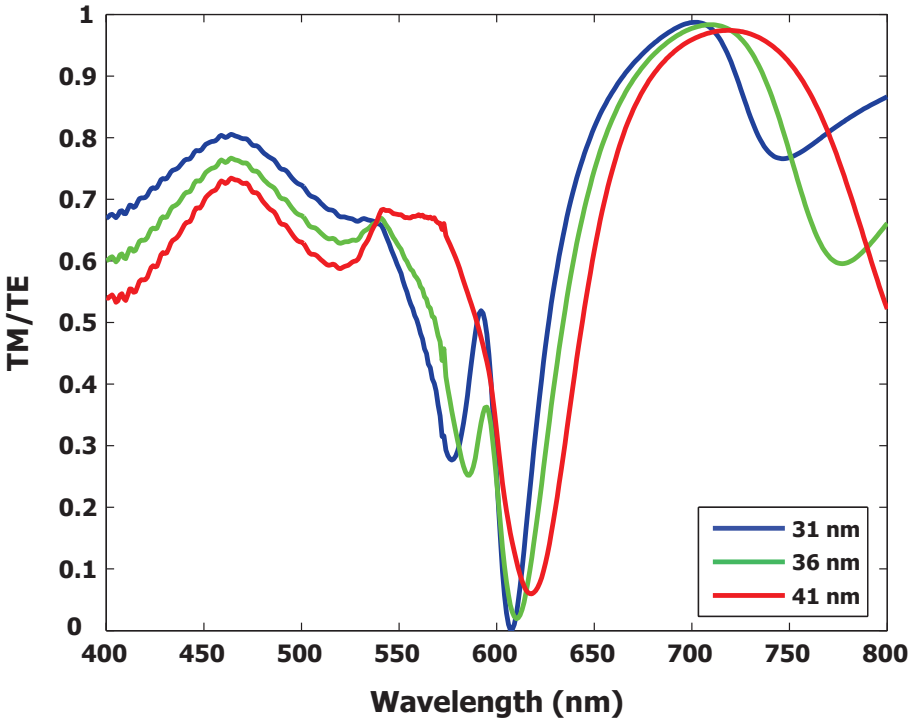

Figure 4.9: TM to TE ratio as a function of wavelength and grating depth simulated by PhotonicsSHA 2D for a 430 nm grating period with different depths.

Chapter 5 : Conclusion and Future Work

5.1 Conclusion

Over the last five decades, SPR sensors have gained great interest, as they introduce label free sensors with real time sensing. Various approaches have been reported for SPR excitation and sensing: single or multi-mode. This document provides basic level understanding of SPR theory and sensors, as well as an easy method for dual mode SPR excitation using grating structures, where a VP-EBL method was employed for Teflon patterning. Teflon patterning with VP-EBL with chemical development revealed a remarkable improvement for Teflon AF patterning in comparison with direct EBL. A lower clearing dose and full clearance for exposed Teflon AF was observed with this technique. The positive tone behavior with complete Teflon removal can be linked to an induced radiation reaction in the presence of water vapor, or the radiation degradation of Teflon, which is highly dependent on the chamber environment.This method not only provides a very useful mechanism for SPR sensors fabrication, but also for 3D lithography and nano-imprinting. High resolution structures with up to 75 nm half-pitch were patterned on 80 nm thickness samples.

For sensor design, several simulation tools were explored. The advantages and disadvantages of each were addressed and only one packaged converged for the structures considered in this work. A series of experiments were designed to test the SPR supporting structures, and single and dual mode excitation for SPR were observed with this method. The results from these experiments and simulations proved that dual SPR excitation occours, which can be used for self-referencing SPR sensors. In this method, the light is incident from the back of the sensor chip, unlike the grating based SPR, where the light is incident from the top through the analyte, making fluid cell fabrication much easier.

5.2 Future Work

The experimental and simulation results in this work show interesting outcomes, namely Teflon patterning to obtain dual mode SPR excitation. Results can be improved by several approaches. Teflon AF patterning can be improved by studying interaction of Teflon with the electron beam in the presence of water vapor, since little is known in this area. In this work, only one value for the of water vapor pressure was tested (1 Torr). To obtain the process limitations, a range of water vapor pressure could be scanned. The effect of chemical developer (ethanol was used in the present study) is another factor. The reaction of the exposed area with ethanol is unclear, and stronger solvents, such as N-Methyl-2-pyrrolidone (NMP), to examine their effect on the patterns etched into Teflon.

One of the challenges of this work is the simulation. It was difficult to simulate the design with the tools explored:OptiScan, S4 and PhotonicsSHA 2D. PhotonicsSHA 2D was useful for simulations with limited material properties and wavelength range. Testing other simulation tools could improve and make simulations more practical, especially if the material properties can be prescribed by the user. Milling a designated area of the pattern with a focused ion beam (FIB) and imaging the cross section of the grating would give a precise view of the grating shape, making the simulations more accurate. Finally, increasing the Teflon AF thickness and making the light incident with different angles could lead to better results, such as the SPR reflectivity dip width which will improve the sensitivity and LOD.

Appendix A

S4 code for the design in Figure (3.1).

```
S = S4.NewSimulation()
S:SetLattice({350.000000,0.000000},{0.000000,0.000000})
S:SetNumG(100)
S:AddMaterial("BK7", {2.343495,0.000000})
S:AddMaterial("Teflon", {1.735706263,0.000000})
S:AddMaterial("AU_JC", {-1.658092,5.735356})
S:AddMaterial("HO2", {1.792921,0.000000})
S:AddLayer('Layer_Above', 0.000000, 'BK7')
S:AddLayer('layer_1', 500.000000, 'Teflon')
S:AddLayer('layer_2', 50.000000, 'Teflon')
S:SetLayerPatternRectangle('layer_2','AU_JC', {87.50,0.000}, 0.00, {87.50,0.00})
S:AddLayer('layer_3', 50.000000, 'AU_JC')
S:SetLayerPatternRectangle('layer_3','HO2', {87.50,0.00}, 0.00, {87.50,0.00})
S:AddLayer('Layer_Below', 0.000000, 'HO2')
S:SetExcitationPlanewave({0.00,0.00},{0.00,0.00},{1.00,0.00})
frequency = { Frequency vector = 1/wavelength};
real_eps_1 = {BK7 real part of the dielectric constant for the frequency vector};
imag_eps_1 = { BK7 imaginary part of the dielectric constant for the frequency vector};
real_eps_2 = {Teflon AF real part of the dielectric constant for the frequency vector};
imag_eps_2 = {Teflon imaginary part of the dielectric constant for the frequency vector};
real_eps_3 = {gold real part of the dielectric constant for the frequency vector};
imag_eps_3 = {gold imaginary part of the dielectric constant for the frequency vector};
real_eps_4 = {water real part of the dielectric constant for the frequency vector};
imag_eps_4 = {water imaginary part of the dielectric constant for the frequency vector};
for i = 1, 601 do
        freq = frequency[i];
        S:SetFrequency(freq)
        S:SetMaterial('BK7', {real_eps_1[i], imag_eps_1[i]});
        S:SetMaterial('Teflon', {real_eps_2[i], imag_eps_2[i]});
        S:SetMaterial('AU_JC', {real_eps_3[i], imag_eps_3[i]});
        S:SetMaterial('HO2', {real_eps_4[i], imag_eps_4[i]});
        incidence_flux, reflection_flux_BK7 = S:GetPoyntingFlux('Layer_Above', 0.000000)
        reflection_flux_BK7 = (-1) * reflection_flux_BK7 / incidence_flux;
        transmission_flux = S:GetPoyntingFlux('Layer_Below', 0.000000)
        transmission_flux_HO2 = transmission_flux / incidence_flux;
        incidence_flux_BK7 = incidence_flux / incidence_flux;
        print(1/freq .. '\t' .. reflection_flux_BK7);
end
```

References

[1] H. Zhang and S. G. Weber, *Fluorous Chemistry*. Springer Berlin Heidelberg, 2012, vol. 308, ch. Teflon AF material, pp. pp 307–337.

[2] R. W. Wood, "Xlii. on a remarkable case of uneven distribution of light in a diffraction grating spectrum," *The London, Edinburgh, and Dublin Philosophical Magazine and Journal of Science.*, vol. 4, no. 21, pp. 396–402., 1902.

[3] T. Turbadar, "Complete absorption of light by thin metal films." *Proceedings of the Physical Society*, vol. 73, no. 1, pp. 40–44, 1959.

[4] A. Otto, "Excitation of nonradiative surface plasma waves in silver by the method of frustrated total reflection." *Zeitschrift für Physik*, vol. 216, no. 4, pp. 398–410, 1968. [Online]. Available: http://dx.doi.org/10.1007/BF01391532

[5] Z. Salamon and G. Tollin, "Surface plasmon resonance, theory," vol. 3, pp. 2804–2812, 1999.

[6] K. Erwin and H. Raether, "Radiative decay of non-radiative surface plasmons excited by light," *Z. Naturforsch. a*, vol. 23, no. 12, pp. 2135–2136, 1968.

[7] R. H. Ritchie *et al.*, "Surface-plasmon resonance effect in grating diffraction," *Physical Review Letters*, vol. 21, no. 22, pp. 1530–1533, November 1968. [Online]. Available: http://link.aps.org/doi/10.1103/PhysRevLett.21.1530

[8] J. DostÃ¡lek *et al.*, "Surface plasmon resonance biosensor based on integrated optical waveguide," *Sensors and Actuators B: Chemical*, vol. 76, no. 1-3, pp. 8 – 12, 2001, proceeding of the Eighth International Meeting on Chemical Sensors IMCS-8 - Part 1. [Online]. Available: http://www.sciencedirect.com/science/article/pii/S0925400501005597

[9] P. B. Johnson and R. W. Christy, "Optical constants of the noble metals," *Phys. Rev. B*, vol. 6, pp. 4370–4379, Dec 1972. [Online]. Available: http://link.aps.org/doi/10.1103/PhysRevB.6.4370

[10] *Data sheet for N-BK7*, SCHOTT north America Inc., 2007.

[11] J. H. Lowry *et al.*, "Optical characteristics of the teflon af fluoro-plastic materials," pp. 142–151, 1991. [Online]. Available: http://dx.doi.org/10.1117/12.47534

[12] R. Slavík *et al.*, "Advanced biosensing using simultaneous excitation of short and long range surface plasmons," *Measurement Science and Technology*, vol. 17, no. 4, pp. 932–938, 2006.

[13] J. T. Hastings *et al.*, "Optimal self-referenced sensing using long- and short- range surface plasmons," *Optical Society of America*, 2007.

[14] M. Vala *et al.*, "Diffraction grating-coupled surface plasmon resonance sensor based on spectroscopy of long-range and short-range surface plasmons," 2007. [Online]. Available: http://dx.doi.org/10.1117/12.723131

[15] J. G. II and S. Ernst, "Surface plasmons as a probe of the electrochemical interface," *Surface Science*, vol. 101, no. 1-3, pp. 499 – 506, 1980. [Online]. Available: http://www.sciencedirect.com/science/article/pii/0039602880906445

[16] O. S.Wolfbeis, *Surface Plasmon Resonance Based Sensors*, ser. Springer Series On Chemical Sensor And Biosensor, H. J., Ed. Springer, 2006, vol. 4.

[17] M. W. Denhoff and M. Gao, "Patterning amorphous fluoropolymer films by reactive ion milling," *M. W. Denhoff*, vol. 26, no. 8, pp. 941–943, 1997. [Online]. Available: http://dx.doi.org/10.1007/s11664-997-0278-2

[18] V. Karre *et al.*, "Direct electron-beam patterning of teflon af," *IEEE TRANSACTIONS ON NANOTECHNOLOGY*, vol. 8, no. 2, pp. 139–141, 2009.

[19] I. Czolkos *et al.*, "High-resolution micropatterned teflon af substrates for biocompatible nanofluidic devices," *Langmuir*, vol. 28, no. 6, pp. 3200–3205, 2012. [Online]. Available: http://pubs.acs.org/doi/abs/10.1021/la2044784

[20] A. Jesorka and M. Shaali, "Lithographic pattern development process for amorphous fluoropolymer," U.S. Patent US20 140 065 551 A1, 2014. [Online]. Available: http://www.google.com/patents/US20140065551

[21] W. Bűrger *et al.*, "Radiation degradation of fluoropolymers: Carboxylated fluoropolymers from radiation degradation in presence of air," *Journal of Applied Polymer Science*, vol. 48, no. 11, pp. 1973–1985, June 1993.

[22] T. Milster, "Optiscan," 2012. [Online]. Available: http://www.optics.arizona.edu/Milster/optiscan/OptiScan_MENU_PAGE.htm

[23] J. Kang *et al.*, "S4: Stanford stratified structure solver," Apr 2013. [Online]. Available: https://nanohub.org/resources/15167

[24] X. Ni *et al.*, "Photonicssha-2d: Modeling of single-period multilayer optical gratings and metamaterials," Aug 2009. [Online]. Available: https://nanohub.org/resources/6977

[25] M. G. Moharam and T. K. Gaylord, "Rigorous coupled-wave analysis of planar-grating diffraction," *J. Opt. Soc. Am.*, vol. 71, no. 7, pp. 811–818, Jul 1981. [Online]. Available: http://www.opticsinfobase.org/abstract.cfm?URI=josa-71-7-811

[26] P. D. Keathley and J. T. Hastings, "Nano-gap-enhanced surface plasmon resonance sensors," *Plasmonics*, vol. 7, pp. 59–69, 2012.

Vita

Mansoor Sultan was born in Bayji, Iraq. He received his B.Eng from the department of medical instrumentations engineering at the Technical college of Mosul in Nenevah, Iraq. He worked for 7 years at Bayji Gas power plant in Bayji, Iraq, as an operation engineer. In 2010, he got a sponsorship from Higher Committee for Education in Iraq (HCED) to pursue a Master of Science (M.Sc) degree in Electrical Engineering. He started his M.Sc in Electrical Engineering at the University of Kentucky, in Lexington, in August 2013.